MAPPING INVASIVE PLANTS USING RPAS AND REMOTE SENSING

By

JACKSON PHILIP JEROME BARON

B.A., Thompson Rivers University 2017

A THESIS SUBMITTED IN PARTIAL FULFILLMENT OF THE REQUIREMENTS FOR THE DEGREE OF MASTER OF SCIENCE IN ENVIRONMENTAL SCIENCE

Thesis examining committee:

David Hill (PhD), Associate Professor and Thesis Supervisor, Department of Geography and Environmental Studies, Thompson Rivers University

Haytham El Miligi (PhD), Associate Professor and Committee Member, Department of Computing Science, Thompson Rivers University

John Church (PhD), Associate Professor and Committee Member, Department of Natural Resource Science, Thompson Rivers University

Catherine Tarasoff (PhD), Adjunct Professor and (Unofficial) Committee Member, Department of Natural Resource Science, Thompson Rivers University

Ashlin Richardson (MSc), Senior Data Scientist and External Member, Office of the Chief Information Officer, Province of British Columbia

Fall 2020

Thompson Rivers University

© Jackson Philip Jerome Baron 2020

Abstract

The ability to accurately detect invasive plant species is integral in their management, treatment, and removal. This study focused on developing and evaluating RPAS-based methods for detecting invasive plant species using image analysis and machine learning and was conducted in two stages. First, supervised classification to identify the invasive yellow flag iris (*Iris pseudacorus*) was performed in a wetland environment using high-resolution raw imagery captured with an uncalibrated visible-light camera. Colour-thresholding, template matching, and de-speckling prior to training a random forest classifier are explored in terms of their benefits towards improving the resulting classification of YFI plants within each image. The impacts of feature selection prior to training are also explored. Results from this work demonstrate the importance of performing image processing and it was found that the application of colour thresholding and de-speckling prior to classification by a random forest classifier trained to identify patches of YFI using spectral and textural features provided the best results. Second, orthomosaicks generated from multispectral imagery were used to detect and predict the relative abundance of spotted knapweed (*Centaurea maculosa*) in a heterogeneous grassland ecosystem. Relative abundance was categorized in qualitative classes and validated through field-based plant species inventories. The method developed for this work, termed metapixel-based image analysis, segments orthomosaicks into a grid of metapixels for which grey-level co-occurrence matrix (GLCM)-based statistics can be computed as descriptive features. Using RPAS-acquired multispectral imagery and plant species inventories performed on $1m^2$ quadrats, a random forest classifier was trained to predict the qualitative degree of spotted knapweed ground-cover within each metapixel. Analysis of the performance of metapixel-based image analysis in this study suggests that feature optimization and the use of GLCM-based texture features are of critical importance for achieving an accurate classification. Additional work to further test the generalizability of the detection methods developed is recommended prior to deployment across multiple sites.

Keywords: Remote sensing; Remotely piloted aircraft systems (RPAS); Invasive plant species; *Iris pseudacorus*; *Centaurea maculosa*; Machine learning; Random forest; Grey-level co-occurrence matrix

Table of Contents

Acknowledgements

I would like to thank my committee members: my supervisor David Hill for his mentorship, expert guidance and support throughout the duration of my academic career; Catherine Tarasoff for her time helping find and establish a research site, and her patience as I learned to view this as an ecological study as well as a remote sensing one; Haytham El Miligi for providing me with a strong foundation for practicing machine learning, and coaching me through the early phases of development; John Church for providing his research equipment, recommendations, and valuable feedback; and Ashlin Richardson for his time, effort, and thoughtful consideration as the external examiner for my thesis defense.

I would also like to thank everyone in the GeoX Lab for providing and supporting a productive and enjoyable workspace. In particular, I'd like to thank Brandon Turner for his help problem solving and troubleshooting coding issues; Jaimie Shippit for her expert advice regarding anything and everything GIS related; and Anika Battel for her time spent out in the field performing plant species inventories.

Finally, I would like to thank my wife, Olivia, for her never-ending patience and support throughout this entire process. I would not have been able to do this without her help.

This research was funded by grants to David Hill from the National Science and Engineering Research Council. I was also supported through an NSERC Canadian Graduate Scholarship – Master's Level, and a Mitacs Accelerate internship.

List of Figures

List of Tables

List of Abbreviations

2dRMS	Twice the Distance Root Mean Square
ASM	Angular Second Moment
BC	British Columbia
CPU	Central Processing Unit
CVWMA	Creston Valley Wildlife Management Area
DS	De-Speckling
EER	Equal Error Rate
EXIF	Exchangeable Image File
FN	False Negative
FP	False Positive
FWHM	Full Width, Half Maximum
GB	Gigabyte
GCP	Ground Control Points
GIS	Geographic Information System
GIMP	GNU Image Manipulation Program
GLCM	Grey-Level Co-Occurrence Matrix
GNSS	Global Navigation Satellite System
GPS	Global Positioning System
GRD	Ground-Resolved Distance
Ha	Hectares
HSV	Hue, Saturation, Value
LGMGIS	Laurie Guichon Memorial Grasslands Interpretive Site
LiDAR	Light Distance and Ranging
MODIS	Moderate Resolution Imaging Spectroradiometer
NDVI	Normalized Difference Vegetation Index
NIR	Near Infrared
OA	Overall Accuracy
OBIA	Object-Based Image Analysis
P	Precision
RAM	Random-Access Memory
RGB	Red, Blue, Green
RPAS	Remotely Piloted Aircraft System
S	Sensitivity
SBAS	Satellite-Based Augmentation System
SfM	Structure from Motion
SFOC	Special Flight Operations Certification
TM	Template Matching
TN	True Negative
TP	True Positive
WAAS	Wide Area Augmentation System
YFI	Yellow Flag Iris

Chapter 1: Introduction

The introduction of remotely piloted aircraft systems (RPAS) as a remote sensing platform has caused a paradigm shift in the acquisition and analysis of geospatial information (Hill, Pypker, and Church, 2019; Vivoni et al., 2014; Wing et al., 2013). RPASs are capable of bridging the scope, scale, and cost differences between surficial measurements and traditional aerial collection methods to provide high-resolution imagery best suited for small scale-mapping operations such as invasive species detection, forest stand management, precision farming, and other environmental applications (Hill, Pypker, and Church, 2019). The availability and relative low-cost of consumer-grade RPASs has lowered the barrier to entry for remote sensing studies, culminating in an increase of data collection, exploratory study, and interdisciplinary research (Simic Milas et al., 2018; González-Jorge, Martínez-Sánchez, and Bueno, 2017). The results of this work have helped elucidate many of the capabilities, as well as the limitations, of varying RPAS platform and sensor configurations for remote sensing applications in the fields of invasive species management, machine learning, and image analysis (e.g., Qian et al., 2020; Wijesingha et al., 2020; Abeysinghe et al., 2019; Dash et al., 2019; Sandino, Mengerson, and Gaston, 2018; Alvarez-Taboada, Paredes, and Julián-Pelaz, 2017; Hill et al., 2017).

Remotely Piloted Aircraft Systems

Exploration of RPASs as a sensing platform has in-part focused on application-based experimentation and development of research methods in which land-cover mapping is being performed at high spatial resolutions relative to aerial and satellite imagery (Adão et al., 2017). Additionally, RPAS mapping has enabled more comprehensive data collection in small-scale applications than would be possible with field-based data collection alone (Hill et al., 2017). Considering the relative ease and low cost to conduct RPAS-based remote sensing, data collection can occur with increased frequency compared to aerial and satellite methods while also covering greater spatial extents than possible with traditional field-based methods (Hill & Babbar-Sebens, 2019; Colomina & Molina, 2014; Vivoni et al., 2014; Wing et al., 2013). The use of RPASs in conjunction with traditional methods has provided a new

framework in which academic studies can be performed (e.g. Baron & Hill, 2020; Baron, Hill, and Elmiligi, 2018; Hill et al., 2017).

RPASs as a research tool have a unique set of benefits and limitations. From a remote sensing standpoint, it is inexpensive to fly/re-fly areas of interest, is unobscured by cloud cover, and close to earth measurement allows for high resolution image capture (see the following reviews and the articles referenced therein: Hill, Pypker, and Church 2019; González-Jorge, Martínez-Sánchez, and Bueno, 2017; Vivoni et al., 2014; and Wing et al., 2013). However, there are limitations when compared to other methods. They are susceptible to meteorological conditions such as wind and rain (Shakhatreh et al., 2019; Thibbotuwawa et al., 2019; Wing et al., 2013), and low-to-ground capture introduces risks involving obstacle avoidance and reliability of sensor calibration (Fraga-Lamas et al., 2019; Lim et al., 2019; Wang et al., 2019). From a land management perspective, RPASs excel in being able to perform comprehensive image capture over wide areas and has the capability of doing so frequently (Easterday et al., 2019). Conversely, any collected data must be processed and analysed to extract information from captured imagery and will be less reliable than manually collected field data (Jurjević et al., 2020).

Cost plays a significant role in the effectiveness of RPAS-based remote sensing, as RPASs are a platform and are limited by the hardware/software being employed (Nezami et al., 2020). Leading-edge configurations currently include light distance and ranging (LiDAR) and hyperspectral sensors, variable height flight planning software to maintain sensor calibration, and narrow swath image capture to collect spatially rectified raw imagery(Hill, Pypker, and Church 2019; Gonzalez-Jorge 2017). As such, RPAS-based data collection can occur across a spectrum of costs and considerations. However, by reducing the cost of a platform, the resulting data quality will be impaired (Nezami et al., 2020). Given this impediment, design specifications need to be carefully considered with respect to the available budget and data requirements to optimize the quality of collected data with respect to desired research outcomes (Ganz, Käber, and Adler, 2019; Torresan et al., 2018).

The trend of low-cost remote sensing research is providing wider availability of sensing equipment to researchers, however, this shift to use consumer-grade for research purposes has sparked an interesting debate regarding the validity and reproducibility of the

research being conducted (Rasmussen et al., 2020). Prior to data collection, project planning should consider the reliability of sensing equipment being used, and whether field work is required to ground-truth both the spectral measurements acquired as well as the identification of the targets being studied (Coburn et al., 2018).

Invasive Plant Species

Invasive plants are non-native species that have established and spread in foreign environments, impacting the structure and function of existing ecosystems, and outcompeting existing biotic communities (Pyšek & Richardson, 2010; Qian & Ricklefs, 2006). Detection and treatment are critical in the management and suppression of invasion, as the resulting changes to ecosystems can cause significant negative environmental impacts (Powell, Chase, and Knight, 2011; Davis, 2003). The detection of non-native plants in the early stages of invasion can be difficult, given the often-complex structure of existing ecosystems and the large areas land managers can be tasked with monitoring. However, early detection of invading species has been shown to aid in the overall cost and effectiveness of treatment (Malanson & Walsh, 2013; Holden, Nyrop, and Ellner, 2016). In addition to traditional management practices, such as field-based visual inspections and plant species inventories, remote methods of monitoring and analysis are being explored and implemented.

Invasive plant species mapping poses many applications for the use of RPASs in land management. Satellite and aerial imagery lack the spatial resolution necessary to capture individual small plants within a scene (Baron & Hill, 2020). Large scale analysis has been performed to accurately identify invasion using satellite imagery through ground-cover mapping (Peterson, 2003), however, access to high-resolution imagery has enabled the possible detection and discrete measurement of target species within treatment areas (Martin et al., 2018; Hill et al., 2017; Tamouridou et al., 2017).

The expediency of RPAS-based data collection enables tracking of ecosystem changes within and between growing seasons (Klosterman et al., 2018; Klosterman & Richardson, 2017). Analyses based off RPAS imagery alone won’t have the same level of reliability as field-based manual assessment, however, remote sensing approaches can aid in providing accurate, detailed spatial estimations of invasion than by field-based sampling techniques alone (Kattenborn et al., 2019; Hill et al. 2017). Additionally, the non-invasive

approach to remotely capturing detailed information with RPASs may help mitigate the further spread of invasive species by human carriers in the field.

Machine Learning & Image Analysis

Machine learning is the study of computer algorithms that learn and improve from data (Russell & Norvig, 2002). In conjunction with image analysis, it has been implemented in remote sensing to perform a variety of tasks such as object detection (Cheng, Zhou, and Han, 2016), clustering (Xie et al., 2018), ground-cover mapping (Gibril et al., 2018), and change detection (Gong et al., 2017). The use of machine learning in remote sensing applications has been a target of research for decades (Maxwell, Warner, and Fang, 2018; Lary et al., 2016; Ahmad, Kalra, and Stephen, 2010; Pal & Mather, 2005; Huang & Jensen, 1997). The recent availability of low-cost RPASs has caused a surge in this type of research based on their availability and access to the affordable high-resolution imagery they produce (e.g., Zha et al., 2020; Ampatzidis & Partel, 2019; Li et al., 2019; Zhou et al., 2019; Näsi et al., 2018).

The increased spatial resolution of RPAS-gathered imagery and the spectral resolution of multispectral imagers provides an increased density of measurable characteristics to train classifiers for detection and classification in remote sensing data. While it has been shown that hyperspectral imagery is required to produce accurate predictive models capable of distinguishing vegetative species based on spectral signature alone (Lawrence, Wood, and Sheley, 2006), the capabilities of complex learning algorithms utilizing multispectral imagery paired with texture features calculated using grey-level co-occurrence matrices (GLCMs) (Haralick, Shanmugan, and Dinstein, 1973; Jensen, 2015), have shown promise in identifying specific plant species with RPAS-collected images (Baron & Hill, 2020). Although the wide range of wavelengths within each multispectral band fails to provide strong correlation to an exclusive species within a heterogeneous grassland ecosystem (Dewey, Price, and Ramsey, 1991; Woolley, 1971), optimized classifiers with a robust feature were shown to modest capacity to distinguish a target species within a diverse environmental setting (Baron & Hill, 2020).

Rationale and Research Aims

In order to assess the capabilities of imagery collected with low-cost RPASs and machine learning to identify invasive plant species in natural environments, this work aims to develop methods and data processing workflows to automate the detection of invasive plant species in both raw imagery and orthomosaicks created using the structure-from-motion and multi-view stereo algorithms. In the following chapter (Chapter 2), pixel-based image analysis is utilized to detect yellow flag iris (*Iris pseudacorus*) in a wetland ecosystem using raw images collected with an un-calibrated, visible-light camera. In Chapter 3, metapixel-based image analysis (a subset of object-based image analysis), is used to quantify the relative abundance of spotted knapweed (*Centaurea maculosa*) in a grassland ecosystem using orthomosaicks generated from raw images collected with a calibrated multispectral imager recording in the green, red, red-edge, and near infrared spectral reflectance bands. Chapter 4 will provide a brief summary of the findings of these studies and their implications for research and land management purposes.

REFERENCES

Abeysinghe, T., Simic Milas, A., Arend, K., Hohman, B., Reil, P., Gregory, A., & Vázquez-Ortega, A. (2019). Mapping invasive phragmites australis in the old woman creek estuary using UAV remote sensing and machine learning classifiers. *Remote Sensing*, *11*(11), 1380.

Adão, T., Hruška, J., Pádua, L., Bessa, J., Peres, E., Morais, R., & Sousa, J. J. (2017). Hyperspectral imaging: A review on UAV-based sensors, data processing and applications for agriculture and forestry. *Remote Sensing*, *9*(11), 1110.

Ahmad, S., Kalra, A., & Stephen, H. (2010). Estimating soil moisture using remote sensing data: A machine learning approach. *Advances in Water Resources*, *33*(1), 69-80.

Alvarez-Taboada, F., Paredes, C., & Julián-Pelaz, J. (2017). Mapping of the invasive species Hakea sericea using unmanned aerial vehicle (UAV) and WorldView-2 imagery and an object-oriented approach. *Remote Sensing*, *9*(9), 913.

Ampatzidis, Y., & Partel, V. (2019). UAV-based high throughput phenotyping in citrus utilizing multispectral imaging and artificial intelligence. *Remote Sensing*, *11*(4), 410.

Baron, J., & Hill, D. J. (2020). Monitoring grassland invasion by spotted knapweed (Centaurea maculosa) with RPAS-acquired multispectral imagery. *Remote Sensing of Environment*, *249*, 112008.

Baron, J., Hill, D. J., & Elmiligi, H. (2018). Combining image processing and machine learning to identify invasive plants in high-resolution images. *International Journal of Remote Sensing*, *39*(15-16), 5099-5118.

Cheng, G., Zhou, P., & Han, J. (2016). Learning rotation-invariant convolutional neural networks for object detection in VHR optical remote sensing images. *IEEE Transactions on Geoscience and Remote Sensing*, *54*(12), 7405-7415.

Coburn, C. A., Smith, A. M., Logie, G. S., & Kennedy, P. (2018). Radiometric and spectral comparison of inexpensive camera systems used for remote sensing. *International Journal of Remote Sensing*, *39*(15-16), 4869-4890.

Colomina, I., & Molina, P. (2014). Unmanned aerial systems for photogrammetry and remote sensing: A review. *ISPRS Journal of Photogrammetry and Remote Sensing*, *92*, 79-97.

Dash, J. P., Watt, M. S., Paul, T. S., Morgenroth, J., & Pearse, G. D. (2019). Early detection of invasive exotic trees using UAV and manned aircraft multispectral and LiDAR Data. *Remote Sensing*, *11*(15), 1812.

Davis, M. A. (2003). Biotic globalization: does competition from introduced species threaten biodiversity? *Bioscience*, *53*(5), 481-489.

Dewey, S. A., Price, K. P., & Ramsey, D. (1991). Satellite remote sensing to predict potential distribution of dyers woad (Isatis tinctoria). *Weed Technology*, *5*(3), 479-484.

Easterday, K., Kislik, C., Dawson, T. E., Hogan, S., & Kelly, M. (2019). Remotely sensed water limitation in vegetation: insights from an experiment with unmanned aerial vehicles (UAVs). *Remote Sensing*, *11*(16), 1853.

Fraga-Lamas, P., Ramos, L., Mondéjar-Guerra, V., & Fernández-Caramés, T. M. (2019). A review on IoT deep learning UAV systems for autonomous obstacle detection and collision avoidance. *Remote Sensing*, *11*(18), 2144.

Ganz, S., Käber, Y., & Adler, P. (2019). Measuring tree height with remote sensing—A comparison of photogrammetric and LiDAR data with different field measurements. *Forests*, *10*(8), 694.

Gibril, M. B. A., Idrees, M. O., Shafri, H. Z. M., & Yao, K. (2018). Integrative image segmentation optimization and machine learning approach for high quality land-use and land-cover mapping using multisource remote sensing data. *Journal of Applied Remote Sensing*, *12*(1), 016036.

Gong, M., Zhan, T., Zhang, P., & Miao, Q. (2017). Superpixel-based difference representation learning for change detection in multispectral remote sensing images. *IEEE Transactions on Geoscience and Remote sensing*, *55*(5), 2658-2673.

González-Jorge, H., Martínez-Sánchez, J., & Bueno, M. (2017). Unmanned aerial systems for civil applications: A review. *Drones*, *1*(1), 2.

Haralick, R. M., Shanmugam, K., & Dinstein, I. H. (1973). Textural features for image classification. *IEEE Transactions on systems, man, and cybernetics*, (6), 610-621.

Hill, D. J., & Babbar-Sebens, M. (2019). Promise of UAV-assisted adaptive management of water resources systems. *Journal of Water Resources Planning and Management*, *145*(7), 02519001.

Hill, D. J., Pypker, T. G., & Church, J. (2020). Applications of unpiloted aerial vehicles (UAVs) in forest hydrology. In *Forest-Water Interactions* (pp. 55-85). Springer, Cham.

Hill, D. J., Tarasoff, C., Whitworth, G. E., Baron, J., Bradshaw, J. L., & Church, J. S. (2017). Utility of unmanned aerial vehicles for mapping invasive plant species: a case study on yellow flag iris (Iris pseudacorus L.). *International Journal of Remote Sensing*, *38*(8-10), 2083-2105.

Holden, M. H., Nyrop, J. P., & Ellner, S. P. (2016). The economic benefit of time-varying surveillance effort for invasive species management. *Journal of Applied Ecology*, *53*(3), 712-721.

Huang, X., & Jensen, J. R. (1997). A machine-learning approach to automated knowledge-base building for remote sensing image analysis with GIS data. *Photogrammetric Engineering and Remote Sensing*, *63*(10), 1185-1193.

Jensen, J. R. (1996). *Introductory digital image processing: a remote sensing perspective* (No. Ed. 2). Prentice-Hall Inc.

Jurjević, L., Liang, X., Gašparović, M., & Balenović, I. (2020). Is field-measured tree height as reliable as believed–Part II, A comparison study of tree height estimates from conventional field measurement and low-cost close-range remote sensing in a deciduous forest. *ISPRS Journal of Photogrammetry and Remote Sensing*, *169*, 227-241.

Kattenborn, T., Lopatin, J., Förster, M., Braun, A. C., & Fassnacht, F. E. (2019). UAV data as alternative to field sampling to map woody invasive species based on combined Sentinel-1 and Sentinel-2 data. *Remote Sensing of Environment*, *227*, 61-73.

Klosterman, S., Melaas, E., Wang, J. A., Martinez, A., Frederick, S., O'Keefe, J., ... & Friedl, M. (2018). Fine-scale perspectives on landscape phenology from unmanned aerial vehicle (UAV) photography. *Agricultural and Forest Meteorology*, *248*, 397-407.

Klosterman, S., & Richardson, A. D. (2017). Observing spring and fall phenology in a deciduous forest with aerial drone imagery. *Sensors*, *17*(12), 2852.

Lary, D. J., Alavi, A. H., Gandomi, A. H., & Walker, A. L. (2016). Machine learning in geosciences and remote sensing. *Geoscience Frontiers*, *7*(1), 3-10.

Lawrence, R. L., Wood, S. D., & Sheley, R. L. (2006). Mapping invasive plants using hyperspectral imagery and Breiman Cutler classifications (RandomForest). *Remote Sensing of Environment*, *100*(3), 356-362.

Li, J., Yang, B., Cong, Y., Cao, L., Fu, X., & Dong, Z. (2019). 3D forest mapping using a low-cost UAV laser scanning system: Investigation and comparison. *Remote Sensing*, *11*(6), 717.

Lim, P. C., Seo, J., Son, J., & Kim, T. (2019). Analysis of orientation accuracy of an UAV image according to camera calibration. *The International Archives of Photogrammetry, Remote Sensing and Spatial Information Sciences*, 437-442.

Malanson, G. P., & Walsh, S. J. (2013). A geographical approach to optimization of response to invasive species. In *Science and Conservation in the Galapagos Islands* (pp. 199-215). Springer, New York, NY.

Martin, F. M., Müllerová, J., Borgniet, L., Dommanget, F., Breton, V., & Evette, A. (2018). Using single-and multi-date UAV and satellite imagery to accurately monitor invasive knotweed species. *Remote Sensing*, *10*(10), 1662.

Maxwell, A. E., Warner, T. A., & Fang, F. (2018). Implementation of machine-learning classification in remote sensing: An applied review. *International Journal of Remote Sensing*, *39*(9), 2784-2817.

Näsi, R., Honkavaara, E., Blomqvist, M., Lyytikäinen-Saarenmaa, P., Hakala, T., Viljanen, N., ... & Holopainen, M. (2018). Remote sensing of bark beetle damage in urban forests at individual tree level using a novel hyperspectral camera from UAV and aircraft. *Urban Forestry & Urban Greening*, *30*, 72-83.

Nezami, S., Khoramshahi, E., Nevalainen, O., Pölönen, I., & Honkavaara, E. (2020). Tree species classification of drone hyperspectral and rgb imagery with deep learning convolutional neural networks. *Remote Sensing*, *12*(7), 1070.

Pal, M., & Mather, P. M. (2005). Support vector machines for classification in remote sensing. *International Journal of Remote Sensing*, *26*(5), 1007-1011.

Peterson, E. B. (2003). Mapping percent-cover of the invasive species Bromus tectorum (cheatgrass) over a large portion of Nevada from satellite imagery. *Report for the US Fish and Wildlife Service, Nevada State Office, Reno, by the Nevada Natural Heritage Program, Carson City*.

Powell, K. I., Chase, J. M., & Knight, T. M. (2011). A synthesis of plant invasion effects on biodiversity across spatial scales. *American Journal of Botany*, *98*(3), 539-548.

Pyšek, P., & Richardson, D. M. (2010). Invasive species, environmental change and management, and health. *Annual review of environment and resources*, *35*.

Qian, W., Huang, Y., Liu, Q., Fan, W., Sun, Z., Dong, H., ... & Qiao, X. (2020). UAV and a deep convolutional neural network for monitoring invasive alien plants in the wild. *Computers and Electronics in Agriculture*, *174*, 105519.

Qian, H., & Ricklefs, R. E. (2006). The role of exotic species in homogenizing the North American flora. *Ecology Letters*, *9*(12), 1293-1298.

Rasmussen, J., Azim, S., Boldsen, S. K., Nitschke, T., Jensen, S. M., Nielsen, J., & Christensen, S. (2020). The challenge of reproducing remote sensing data from satellites and unmanned aerial vehicles (UAVs) in the context of management zones and precision agriculture. *Precision Agriculture*, 1-18.

Russell, S., & Norvig, P. (2002). Artificial intelligence: a modern approach.

Sandino, J., Gonzalez, F., Mengersen, K., & Gaston, K. J. (2018). UAVs and machine learning revolutionising invasive grass and vegetation surveys in remote arid lands. *Sensors*, *18*(2), 605.

Shakhatreh, H., Sawalmeh, A. H., Al-Fuqaha, A., Dou, Z., Almaita, E., Khalil, I., ... & Guizani, M. (2019). Unmanned aerial vehicles (UAVs): A survey on civil applications and key research challenges. *IEEE Access*, *7*, 48572-48634.

Simic Milas, A., Sousa, J. J., Warner, T. A., Teodoro, A. C., Peres, E., Gonçalves, J. A., ... & Woodget, A. (2018). Unmanned Aerial Systems (UAS) for environmental applications special issue preface. *International Journal of Remote Sensing*, *39*(15-16), 4845-4851.

Tamouridou, A. A., Alexandridis, T. K., Pantazi, X. E., Lagopodi, A. L., Kashefi, J., & Moshou, D. (2017). Evaluation of UAV imagery for mapping Silybum marianum weed patches. *International Journal of Remote Sensing*, *38*(8-10), 2246-2259.

Thibbotuwawa, A., Bocewicz, G., Nielsen, P., & Banaszak, Z. (2019). UAV Mission Planning Subject to Weather Forecast Constraints. In *International Symposium on Distributed Computing and Artificial Intelligence* (pp. 65-76). Springer, Cham.

Torresan, C., Berton, A., Carotenuto, F., Chiavetta, U., Miglietta, F., Zaldei, A., & Gioli, B. (2018). Development and performance assessment of a low-cost UAV laser scanner system (LasUAV). *Remote Sensing*, *10*(7), 1094.

Vivoni, E. R., Rango, A., Anderson, C. A., Pierini, N. A., Schreiner-McGraw, A. P., Saripalli, S., & Laliberte, A. S. (2014). Ecohydrology with unmanned aerial vehicles. *Ecosphere*, *5*(10), 1-14.

Wijesingha, J., Astor, T., Schulze-Brueninghoff, D., & Wachendorf, M. (2020). Mapping invasive Lupinus polyphyllus Lindl. in semi-natural grasslands using object-based image analysis of UAV-borne images. *PFG–Journal of Photogrammetry, Remote Sensing and Geoinformation Science*, *88*(5), 391-406.

Wang, L., Lan, Y., Zhang, Y., Zhang, H., Tahir, M. N., Ou, S., ... & Chen, P. (2019). Applications and prospects of agricultural unmanned aerial vehicle obstacle avoidance technology in China. *Sensors*, *19*(3), 642.

Wing, M. G., Burnett, J., Sessions, J., Brungardt, J., Cordell, V., Dobler, D., & Wilson, D. (2013). Eyes in the sky: Remote sensing technology development using small unmanned aircraft systems. *Journal of Forestry*, *111*(5), 341-347.

Woolley, J. T. (1971). Reflectance and transmittance of light by leaves. *Plant Physiology*, *47*(5), 656-662.

Xie, H., Zhao, A., Huang, S., Han, J., Liu, S., Xu, X., ... & Tong, X. (2018). Unsupervised hyperspectral remote sensing image clustering based on adaptive density. *IEEE Geoscience and Remote Sensing Letters*, *15*(4), 632-636.

Zha, H., Miao, Y., Wang, T., Li, Y., Zhang, J., Sun, W., ... & Kusnierek, K. (2020). Improving unmanned aerial vehicle remote sensing-based rice nitrogen nutrition index prediction with machine learning. *Remote Sensing*, *12*(2), 215.

Zhou, C., Ye, H., Xu, Z., Hu, J., Shi, X., Hua, S., ... & Yang, G. (2019). Estimating maize-leaf coverage in field conditions by applying a machine learning algorithm to UAV remote sensing images. *Applied Sciences*, *9*(11), 2389.

Chapter 2: Combining Image Processing and Machine Learning to Identify Invasive Plants in High Resolution Images

INTRODUCTION

Invasive plants are non-native species that outcompete existing native species when introduced to new environments, altering the existing ecosystem and homogenizing biotic communities (Pyšek & Richardson, 2010; Qian & Ricklefs, 2006). Invasion by invasive species can trigger rapid change in an ecosystem and result in significant negative environmental impacts (Hawthorne et al., 2015; Fernandes et al., 2014). Freshwater ecosystems are particularly vulnerable, as natural, or human-induced forces are common within these ecosystems and can result in significant changes to the ecosystem (Havel et al., 2015). The treatment and removal of invasive species is critical in reversing their ecological impact. Early detection of invasions and mapping the extent of invasions are crucial steps toward this goal (Adam, Mutanga, and Rugege, 2010; Malanson & Walsh, 2013).

Remote sensing in land management and invasive species mapping has become increasingly popular with the introduction of remotely piloted aircraft systems (RPASs) as a sensing platform (e.g., Hill et al., 2017; Kraaijenbrink et al., 2016; Ma et al., 2015; Mathews, 2014; Michez et al., 2016; Moranduzzo et al., 2015; Moranduzzo & Melgani, 2014; Pérez-Ortiz et al., 2016). RPASs are valuable for land management applications, from ground mapping and vegetation type identification to vegetation species mapping for monitoring and inventory purposes, due to their low investment costs and to the high resolution of images they can produce (Yu et al., 2016; Pérez-Ortiz et al., 2016; Hill et al., 2017). Our previous work (Hill et al., 2017) compared the performance of manual and automated image analysis to traditional field methods for mapping the extent of invasion of a wetland ecosystem by the species yellow flag iris (YFI) (*Iris pseudacorus* L.). This previous work demonstrated that manual interpretation of raw colour images acquired by the digital camera integrated into an off-the-shelf consumer-grade RPAS provided a more accurate estimate of the location and extent of YFI invasion than either traditional field methods or automated pixel-based classification by a random forest classifier. Traditional field methods tended to underestimate the areal extent of the YFI invasion, while the pixel-based classification of the

orthomosaicked colour images tended to overestimate the extent of YFI invasion, due to false positive classifications. Furthermore, the use of orthomosaicked images obscured YFI invasion that was obscured by overlying cover, such as tree canopies.

This study expands our previous work by exploring hybrid image classification methods that combine image processing and machine learning tools to more accurately identify YFI in a colour image acquired by an un-calibrated digital camera with 1-byte encoding for each of the three bands (red, green, and blue) recorded. Building on our previous work (Hill et al., 2017), which demonstrated that orthomosaicking can obscure YFI growing below the tree canopy and, thus, lead to underestimation of the extent of an invasion, this work focuses on performing classification of the individual images acquired by the digital camera, which retain the perspective projection of a typical photograph. Furthermore, our previous work suggested that eliminating areas unlikely to contain YFI from the pixel-based classification, by masking deep water and tree-tops, improved the classification performance.

In the present paper, we investigate combinations of image processing tools to more precisely mask areas of the image unlikely to contain YFI. Specifically, we consider images pre-processed by colour thresholding, template matching, and/or de-speckling before classification by a supervised random forest model. We also explore the use of feature selection by recursive feature elimination for improving the performance of the random forest classifier. The following section of this paper describes the study site where the images were acquired. Next, the methods of image acquisition and data preparation, image processing, classification, and performance evaluation will be discussed. Results from the classifications are then presented and discussed, and finally, conclusions are provided detailing the effectiveness of methods used in improving identification of YFI in images collected by RPAS-borne digital cameras.

STUDY SITE

The area investigated in this study is the Creston Valley Wildlife Management Area (CVWMA), located south of Kootenay Lake in the interior of British Columbia (BC), Canada. Figure 2.1 shows the location of the CVWMA, in relation to Vancouver, BC's

largest city. The CVWMA covers 7,000 hectares, including one 15-hectare lake, 17 marshes, and a major river extending between the adjacent Selkirk and Purcell mountain ranges (Creston Valley Wildlife Management Area, n.d.). The area provides critical support for a multitude of biologically diverse species, including many species of birds, mammals, fish, reptiles, amphibians, invertebrates, and plants. The high density of lakes, rivers, and marshes creates a hospitable environment for YFI to invade and spread. All images considered in this work were acquired in regions of the CVWMA known to be infested with YFI.

Figure 2.1: Location of the Creston Valley Wildlife Management Area in relation to Vancouver within the province of British Columbia, Canada. Map is rendered in the BC Environmental Albers Equal Area Conic projection.

METHODS

All data analysis was performed using Anaconda, a free and open-source distribution of the Python Programming Language, as well as the Scikit-Image 0.13.0 image processing libraries, the OpenCV computer vision libraries, the Scikit-Learn 0.18 machine learning libraries, and ArcMap 10.2.

Image Acquisition and Data Preparation

The images used in this study were collected from the CVWMA on 6 June 2015 using a DJI Phantom 3 Professional equipped with an un-calibrated 12.4-megapixel digital

camera. The date of acquisition was selected to minimize intra-stand phenological variability, which is likely to degrade the performance of the image processing and machine learning classifiers explored in this study. Because YFI at the CVWMA typically bloom from late-May to early-July, we expect that during the image acquisition, the YFI was nearly all in bloom. Downward (approximate nadir) imagery was acquired from 71 RPAS missions at an elevation of 30 meters above the land surface. The images were manually split into two categories: scenes containing YFI (939 images) and scenes not containing YFI (1,172 images).

From the subset of images containing YFI, 50 images containing a variety of different image characteristics (e.g. shade, water, roads, buildings, various vegetative species) were selected and used to create a classifier. Another 20 images were then selected at random from the remaining images containing YFI. These latter images were used to generate an independent validation data set for evaluating how the hybrid image-processing/random forest classification methods developed in this study would perform on unseen images.

Reference data for the YFI locations in these 70 images were generated through manual analysis of the imagery and digitization of patches of YFI using ArcMap 10.2, where plants are defined by their digitized boundaries. Our previous work (Hill et al., 2017) demonstrated that manual digitization provided more accurate maps than field surveys did, so these manually digitized images were used as reference data for the location of YFI patches within each image. A geographic information system (GIS) polygon was drawn bounding each YFI cluster within each image, and these polygons were subsequently integrated and converted into a raster layer matching the extent of their respective image. These raster layers indicating the extent of YFI will hereafter be referred to as the YFI reference locations. Figure 2.2 shows an image with YFI outlined in red. Figure 2.3 shows the corresponding mask of YFI locations, where polygons contain both foliage and flowers.

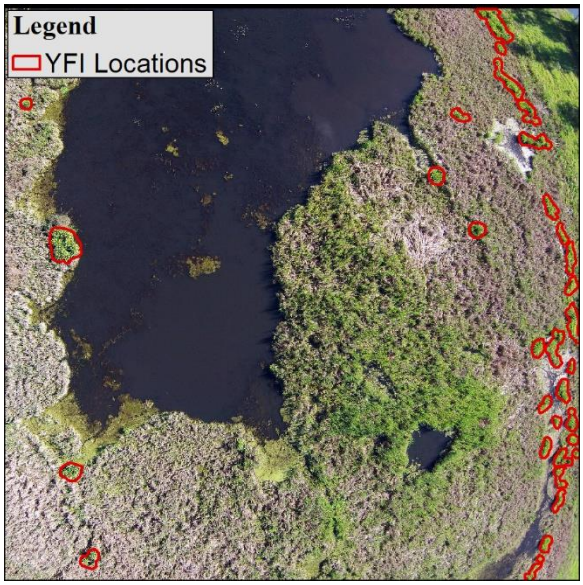

Figure 2.2: A sample image containing yellow flag iris acquired from the Creston Valley Wildlife Management Area. GPS location of camera at point of image capture, 49.1254°N and 116.6277°W.

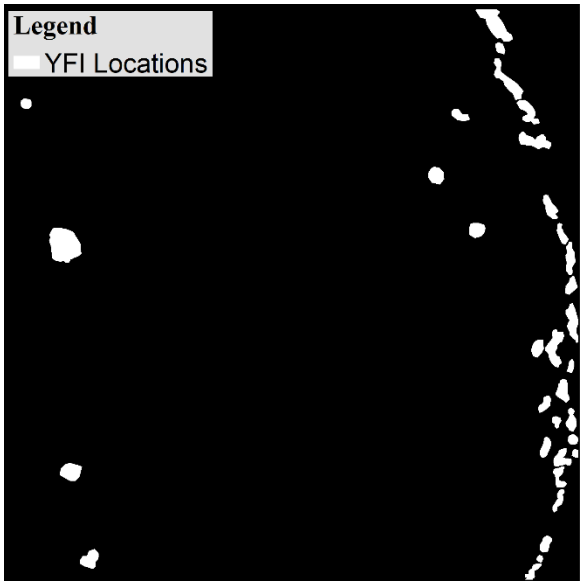

Figure 2.3: An image mask of Figure 2.2, areas in white contain YFI reference locations within the image and areas in black do not. GPS location of camera at point of image capture, 49.1254°N and 116.6277°W.

Image Processing

Colour thresholding was used for image masking on all images considered in this work. When in bloom, YFI displays a bright yellow flower that is approximately 8 centimetres in diameter (Stone, 2009). Because few other yellow objects are found within the study region, the colour yellow can be used to generate a mask that will significantly reduce the amount of data that must be subsequently analysed to identify YFI within an image. Colour thresholding was used to limit the region of the image analysed for containing YFI by the hybrid classification methods and was not used to map the spatial abundance or specific location of each plant independently.

Colour boundaries were selected to filter the raw images to remove areas of the image that do not express the colour yellow. These boundaries were chosen using the hue, saturation, and value (HSV) colour space. The GNU Image Manipulation Program (GIMP) and other image processing programs typically represent hue as 0–360, saturation as 0–100, and value as 0–100 (GNU Image Manipulation Program, n.d.). OpenCV, which was used for this study, stores colour information in a single byte, so hue is represented as 0–180, saturation as 0–255, and value as 0–255. Therefore, although pure yellow is typically represented (e.g. by GIMP) as H = 60, using OpenCV, pure yellow is represented as H = 30. To create the colour threshold, upper and lower bounds were manually tuned through visual analysis to maximize the amount of YFI flowers contained within the mask, while limiting the amount of area that contained similar colour signatures with no YFI. The tuned colour threshold used in this study is the 3-D region of colour space defined in 1-byte HSV as $25 \leq H \leq 35$, $100 \leq S \leq 255$, $100 \leq V \leq 255$.

To mask the images using these colour thresholds, it was first necessary to convert the images to the HSV colour space and mask off pixels displaying colours outside of the region bounded by the colour thresholds. Figure 2.4 illustrates an image with the colour threshold mask applied, and Figure 2.5 displays that image after applying the colour threshold mask and a mask of the YFI reference locations. As can be seen in this image, while the colour threshold mask removes most of the image from further analysis, a considerable amount of the image that corresponds to non-YFI conditions remains unmasked. Thus, further image processing and analysis is required to accurately identify YFI within the

image. To evaluate the importance of further processing the image using template matching and de-speckling prior to classification, experiments were performed using four permutations of the two image processing procedures: (1) neither template matching nor de-speckling, (2) template matching alone, (3) de-speckling alone, and (4) both template matching and de-speckling. Both the template matching and de-speckling procedures are described in detail in the following sub-sections.

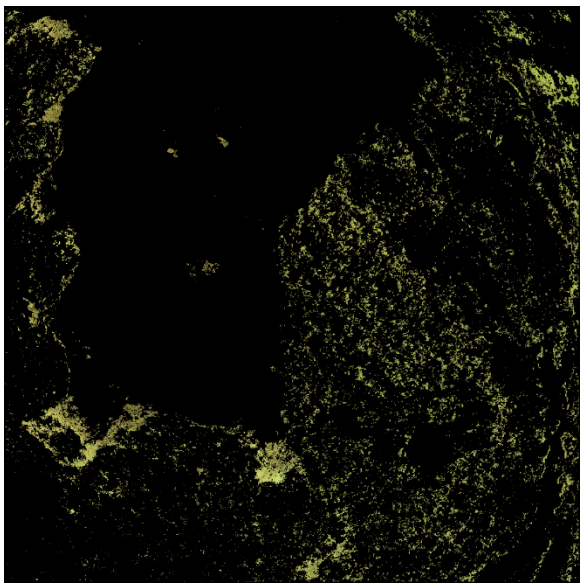

Figure 2.4: A colour threshold mask of Figure 2.2, areas within the colour threshold boundary are displayed in their natural colour and areas in black fall outside colour threshold boundaries. GPS location of camera at point of image capture, 49.1254°N and 116.6277°W.

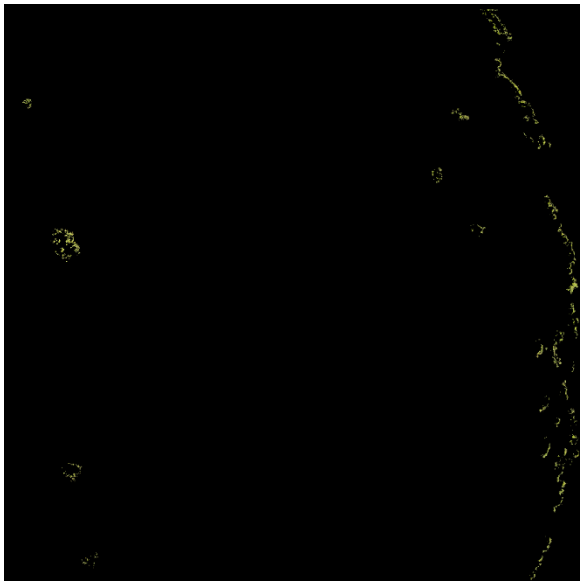

Figure 2.5: The sample image from Figure 2.2 after having a colour threshold mask applied and a mask of YFI reference locations applied. Areas within both the colour threshold boundary and YFI reference locations are displayed in their natural colour, areas outside these bounds are displayed as black. GPS location of camera at point of image capture, 49.1254°N and 116.6277°W.

Template Matching

Template matching searches an image for instances of a template pattern that is characteristic of an object of interest. The template pattern is defined as a rectangle that is w pixels in width and h pixels in height. This template pattern is then compared to each possible $w \times h$ subset of the image. The number of chunks of size $w \times h$ in an image that is W pixels in width and H pixels in height is $(W-w+1) \times (H-h+1)$. Each of these subsets is then compared against the template pattern, and a zero-to-one ranking is calculated for each subset that describes the degree of similarity between the subset and the template pattern. A ranking of 0 indicates that the subset is the most dissimilar of all subsets evaluated, while a ranking of 1 indicates that the subset is the most similar. Positive matches are defined as comparisons in which a subset is ranked above a user-defined similarity threshold value. Subsets that are evaluated to be positive matches to the template pattern are considered to represent areas within the image that contain the object of interest, whereas subsets that are not positive matches are considered regions of the image that do not contain the object of interest.

Through the optimization of the similarity threshold the total number of subsets that result in positive matches yet are not characteristic of the object of interest (i.e. false positive matches), are reduced.

In this study, a template pattern was generated from a 9×9-pixel region of a RPAS-acquired image of the study site that centred on a blooming YFI flower and contained the flower boundaries, defining the flower's shape. The template pattern was further processed by applying the colour thresholding described above and converting the resulting image to greyscale. Pattern matching using this template was performed by first converting an image to greyscale, and then comparing the template pattern to each 9×9-pixel subset of the image. The images in this study were 3,456 pixels in height and 4,608 pixels in width, resulting in 15,860,800 comparisons between the template pattern and subsets of the image.

The similarity threshold was tuned by the equal-error-rate (EER) method. This method compares the false-positive (FP) and false-negative (FN) rates for a classifier against the value of a tuneable parameter, in this case the similarity threshold, and recommends that the optimal value of the parameter is the value of the parameter that results in an equal value of the FP and FN rates. EER was selected for optimization of the similarity threshold over use of a receiver operating curve (ROC) which utilizes the true positive rate (TPR) and false positive rate (FPR) as operating characteristics (Fawcett, 2006). Due to YFI only making up a small proportion of each image, the number of true negative (TN) classifications greatly exceeded all other classifications combined, so the EER method was selected to avoid using TN as a metric and instead focus on minimizing each type of false classification. By searching possible values of the similarity threshold from 0.01 to 0.99, in 0.01-unit steps, the EER was calculated for each of the 50 images selected for creating the classifier. The error rates were computed by comparing the regions of the image identified by template matching to contain YFI against the YFI reference locations for each image. Figure 2.6 illustrates the FP and FN rates versus the similarity threshold as suggested by the EER method. The average value of the optimal similarity threshold computed from 50 images was 0.25, and this value was used as the similarity threshold for processing all the images in the study. Processing an image by template matching removes from the image any regions that do not result in positive template matches, and thus are unlikely to contain YFI.

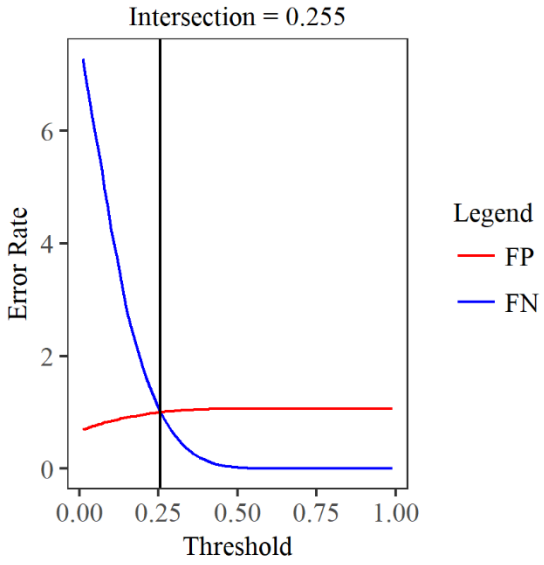

Figure 2.6: A plot illustrating the equal error rate (EER) method for identifying the similarity threshold. These data were calculated for the sample image (Figure 2.2) from the Creston Valley Wildlife Management Area.

De-speckling

The colour threshold and template matching image processing steps serve to focus further analysis of the image on regions that are likely to contain YFI; however, these image processing steps have the tendency to classify single pixels as potentially representing YFI despite these pixels being surrounded by pixels that were classified as being devoid of YFI. De-speckling is a procedure to remove such speckles from an image. In this study, de-speckling was performed by evaluating the image pixel by pixel and switching the classification of any pixel classified as potentially indicating YFI within the image that was not immediately adjacent to at least one pixel that was also positively classified as potentially indicating YFI.

Supervised Classification

Processing the images using colour thresholding, template matching, and de-speckling serves to categorize the image into regions that are likely to contain the target object (i.e. YFI) and those that are not likely to contain the target object. However, there is still more information that can be used to refine the classification based on features derived

from the intensity of red, green, and blue (RGB) colour associated with each pixel. Utilizing this information to its full potential relies on first computing and selecting features derived from these colour intensity values, and then training a supervised classifier to process unseen images.

Generating Training, Testing, and Validation Data

Data sets for supervised training and testing of the random forest classifier were constructed by sampling the YFI reference locations of the 50 images used for creating the hybrid classification method. Zhu et al. (2016) have shown that training a classifier using a balanced training set consisting of an equal number of positive and negative examples improves classifier performance. Thus, both the training and testing data sets were constructed as balanced data sets. This was accomplished using stratified random sampling (as suggested by Ma et al. 2015) to down-sample the majority class (not YFI) and over-sample the minority class (YFI). One training/testing set was created for each case of image processing: (1) colour thresholding only, (2) colour thresholding and template matching, (3) colour thresholding and de-speckling, and (4) colour thresholding, template matching, and de-speckling. Table 2.1 shows the characteristics of each of these four testing/training sets.

Table 2.1: The total number of positive and negative samples generated for the training/testing sets using each of the 4 image processing methods, and the total number of balanced samples used in training/testing. All methods include colour thresholding as a pre-processing step.

Image Processing	Positive Samples	Negative Samples	Total Balanced Samples
Template Matching & De-Speckling	9840	1011369	19680
Template Matching & No De-Speckling	10975	3769554	21950
No Template Matching & De-Speckling	183002	13897850	366004
No Template Matching & No De-Speckling	183002	13897850	366004

Feature Creation

Features derived from the RGB values of each pixel were computed based on a neighbourhood of 9×9 pixels centred at the pixel that is characterized by the derived features. This corresponds to the same neighbourhood used for the template pattern-matching

processing step previously described. Using this neighbourhood, a set of 68 features were created for each pixel positively classified by image processing. These features are based on ten colour measures, namely red intensity, green intensity, blue intensity, HSV hue, HSV saturation, HSV value, grey-scale intensity, excess-red intensity, excess-green intensity, and excess-blue intensity. The excess colour intensity can be computed as:

$$E_{\mathrm{R}} = 2R^* - G^* - B^* \quad (1)$$

$$E_{\mathrm{G}} = 2G^* - R^* - B^* \quad (2)$$

$$E_{\mathrm{B}} = 2B^* - R^* - G^* \quad (3)$$

$$R^* = \frac{R}{R + G + B} \quad (4)$$

$$G^* = \frac{G}{R + G + B} \quad (5)$$

$$B^* = \frac{B}{R + G + B} \quad (6)$$

where R indicates the red band intensity, G indicates the green band intensity, B represents the blue band intensity, E_{R} represents the excess red measure, E_{G} represents the excess green measure, and E_{B} represents the excess blue measure. The excess colour intensities were included in this work because it has been previously shown that these features have been beneficial for distinguishing vegetation species from backdrop vegetation in RGB imagery acquired by a digital camera (Ma et al., 2015). For each of these ten colour features, four statistical features were calculated: the (1) mean, (2) standard deviation, (3) kurtosis, and (4) skew of the colour feature over the pixel neighbourhood. For each of the seven non-HSV colour features, four additional texture features were computed: the (1) contrast, (2) correlation, (3) energy, and (4) homogeneity over the 9×9-pixel neighbourhood. Thus, each pixel that was selected by processing for further analysis is characterized by a total of 68 features based on the 9×9-pixel neighbourhood in which it is centred.

Feature Selection

Recursive feature elimination with 10-fold cross-validation was used to find the optimal subset of the 68 features derived from the recorded RGB values for each pixel. Optimal features were assigned a rank of 1, whereas other features were ranked in increasing order in relation to their performance. To verify the performance of the feature selection, a

classifier was trained and tested with the ranked features using the training data. Classifier performance was recorded for each subset of the highest-ranking features, beginning with the full set of features, and repeating the verification processing until only a single feature remained.

Classification

A random forest classifier was selected for this experiment. It has been used extensively in remote sensing applications (Lawson et al., 2017; Ma et al., 2015; Michez et al., 2016; Mitchell et al., 2016; Rodriguez-Galiano et al., 2012; Zhu et al., 2016) and has performed reasonably well in previous work (Hill et al., 2017). The random forest classifier was trained using 10-fold cross-validation.

Performance Evaluation

Classifier performance was calculated using the metrics of precision, sensitivity, and accuracy. Precision (*P*) was computed on a pixel by pixel basis using the formula:

$$P = \frac{C_{\mathrm{TP}}^{pixel}}{C_{\mathrm{TP}}^{pixel} + C_{\mathrm{FP}}^{pixel}} \tag{7}$$

where C_{TP}^{pixel} is the number of true positive pixel classifications (i.e. pixels representing YFI that are classified as such), and C_{FP}^{pixel} is the number of false positive pixel classifications. Precision was only computed for the validation set, because the balanced data sets used as training and test data would have overestimated precision because they significantly under-represent the number of pixels that do not contain YFI.

Sensitivity (*S*) was measured on a plant-by-plant basis using the formula:

$$S = \frac{C_{\mathrm{TP}}^{plant}}{C_{\mathrm{TP}}^{plant} + C_{\mathrm{FN}}^{plant}} \tag{8}$$

where C_{TP}^{plant} is the number of true positive plant classifications (i.e. an object in the image representing YFI that is classified as such), and C_{FN}^{plant} is the number of false negative plant classifications. Sensitivity was measured on a plant-by-plant basis to evaluate the ability to detect instances of YFI, as opposed to evaluating the ability to accurately detect every pixel contained in a contiguous patch of YFI.

Accuracy was calculated as:

$$A = \frac{C_{\mathrm{TP}}^{pixel} + C_{\mathrm{TN}}^{pixel}}{C_{\mathrm{TP}}^{pixel} + C_{\mathrm{FP}}^{pixel} + C_{\mathrm{FN}}^{pixel} + C_{\mathrm{TN}}^{pixel}} \quad (9)$$

where C_{TP}^{pixel} is the number of true positive pixel classifications, C_{FP}^{pixel} is the number of false positive pixel classifications, C_{FN}^{pixel} is the number of false negative pixel classifications, and C_{TN}^{pixel} is the number of true negative pixel classifications.

These performance measures were computed for classifiers consisting of image processing only and hybrid image-processing/random forest classifiers trained either using feature selection or not using feature selection. C_{TP}^{pixel} was calculated by summing all positively identified pixels within the YFI reference locations, and C_{FP}^{pixel} was all positively identified pixels found outside of the YFI reference locations. C_{FN}^{pixel} was found by subtracting C_{TP}^{pixel} from the total number of pixels contained within the YFI reference locations, and C_{TN}^{pixel} was found by subtracting C_{TP}^{pixel}, C_{FP}^{pixel}, and C_{FN}^{pixel} from the total number of pixels within the image.

RESULTS

In this study, eight hybrid image-processing/random forest classifiers were developed and evaluated to determine the best combination of image processing methods and use of feature selection to identify YFI within aerial images acquired by a RPAS-borne digital camera. Specifically, the hybrid classification methods explored in this study are (1) colour thresholding and no feature selection, (2) colour thresholding and feature selection, (3) colour thresholding, template matching, and no feature selection, (4) colour thresholding, template matching, and feature selection, (5) colour thresholding, de-speckling, and no feature selection, (6) colour thresholding, de-speckling, and feature selection, (7) colour thresholding, template matching, de-speckling, and no feature selection, and (8) colour thresholding, template matching, de-speckling, and feature selection.

Feature Selection

Using recursive feature elimination, an optimum subset of features was determined for each of the test cases incorporating feature selection. For each case, it was found that the optimum number of features to use in creating a classifier was 10. Of these 10 features, 9 were constant for each method, and they included: (1) mean HSV hue, (2) mean HSV

saturation, (3) mean HSV value, (4) standard deviation of HSV hue, (5) standard deviation of HSV saturation, (6) standard deviation of HSV value, (7) kurtosis of HSV saturation, (8) skew of HSV hue, and (9) skew of HSV saturation. For the colour thresholding and template matching test case, the final feature selected was the contrast of blue intensity. For the remaining three cases, the final feature selected was the skew of HSV value.

Classification Performance

A random forest classifier was trained for each of the 8 combinations of image processing using 10-fold cross-validation to train and evaluate the classifier. Table 2.2 contains a table ranking the average accuracy computed across all folds for each of the 8 hybrid classification methods, while training the classifier with the balanced dataset generated from the original 50 images. The classification accuracy computed by the cross-validation was similar for each method, with a mean of 0.82 and a standard deviation of 0.031. The method that used colour thresholding with template matching (but not de-speckling) to process the image that was then classified using a classifier trained using features selected by feature selection scored the highest, with a classification accuracy of 86%. The lowest scoring classification method (77%) was the one that did not perform any additional image processing beyond colour thresholding and did not utilize feature selection to identify an optimal feature set for the random forest classifier.

Table 2.2: Mean 10-fold cross-validation accuracy computed for the balanced training set for each of the hybrid classification methods. All methods include colour thresholding as a pre-processing step.

Image Processing	Feature Selection	Accuracy (%)
Template Matching & No De-Speckling	Yes	86.42
Template Matching & No De-Speckling	No	84.87
No Template Matching & De-Speckling	Yes	82.58
Template Matching & De-Speckling	Yes	81.74
No Template Matching & De-Speckling	No	81.35
Template Matching & De-Speckling	No	80.78
No Template Matching & No De-Speckling	Yes	77.98
No Template Matching & No De-Speckling	No	77.23

The best hybrid classifier created during the training by 10-fold cross-validation was then used with the corresponding processing steps to classify the examples in the balanced

testing set. The accuracy of the hybrid classification methods evaluated on these data is shown in Table 2.3. As was the case during cross-validation using the training set, the method that used colour thresholding, template matching, and feature selection performed the best, with an overall accuracy of 77%. Alternatively, the method that combined colour thresholding, template matching, and de-speckling, but did not use feature selection, had the lowest classification accuracy (67%). The mean was 0.71 with a standard deviation of 0.036. Table 2.3 ranks the accuracy of the 8 hybrid classification methods evaluated in this study for identifying YFI in the test images.

Table 2.3: Average 10-fold cross-validation accuracy of the hybrid classification methods for identifying YFI in test set. All methods include colour thresholding as a pre-processing step.

Image Processing	Feature Selection	Accuracy (%)
Template Matching & No De-Speckling	Yes	77.40
Template Matching & No De-Speckling	No	73.46
No Template Matching & De-Speckling	Yes	71.09
No Template Matching & De-Speckling	No	70.94
Template Matching & De-Speckling	Yes	68.46
No Template Matching & No De-Speckling	Yes	68.10
No Template Matching & No De-Speckling	No	67.95
Template Matching & De-Speckling	No	66.10

Validation

To explore the value of creating hybrid classification methods that combine image processing and machine learning steps, each of the 4 combinations of image processing and each of the 8 hybrid classifiers were evaluated in terms of their accuracy, precision, and sensitivity when tested on the unbalanced validation data set. Table 2.4 shows the accuracy, precision, and sensitivity of the YFI classification for the validation images, computed for the 4 image processing combinations alone and for the 8 hybrid classification methods. As can be seen by these data, all the methods performed well.

The methods with the highest accuracy (>99.3%) were those that used template matching and the random forest classifier. This is likely due to the reduction in the number of false positive classifications made by these, more selective, classifiers. The methods with the lowest accuracy were those that did not use the random forest classifier. The method that processed

the images using colour thresholding, template matching, de-speckling, and used feature selection to guide supervised training performed the best, achieving an accuracy of 99.37%. The method that used colour thresholding only performed the poorest, with a classification accuracy of 98.06%.

The method with the highest classification precision (5.5%) was the method that used only colour thresholding for image processing before applying a supervised classifier trained using the 10 features identified through feature selection. The method that processed images using colour thresholding and template matching and did not use supervised classification had the lowest precision (0.29%).

The maximum number of YFI patches were identified when no further image processing beyond colour thresholding and no supervised classification was applied, with a sensitivity of 95%. This result indicates that 5% of the YFI is excluded due to it not containing any features that were within the limits of the colour threshold. The lowest sensitivity was 35%, when the images were processed by colour thresholding, template matching, and de-speckling prior to supervised classification by a random forest classifier that was trained with all 68 features (no feature selection was used).

Table 2.4: The accuracy, precision, and sensitivity of the combinations of template matching (TM) and De-Speckling (DS) image processing methods alone and hybrid classification methods for classifying the validation data. The highest value for each accuracy, precision, and sensitivity is displayed in bold, and each method is sorted based on the average of the three values. All methods include colour thresholding as a pre-processing step.

Image Processing	Supervised Classification	Feature Selection	Accuracy (%)	Precision (%)	Sensitivity (%)	Average (%)
No TM & DS	Yes	No	99.14	4.83	93.07	65.68
No TM & DS	Yes	Yes	99.15	4.96	92.57	65.56
No TM & No DS	Yes	No	99.19	5.32	92.16	65.56
No TM & DS	No	N/A	98.06	1.67	**94.55**	64.76
No TM & No DS	No	N/A	98.06	1.67	**94.55**	64.76

TM & No DS	Yes	Yes	99.34	1.67	92.08	64.36
TM & No DS	No	N/A	99.04	0.29	91.58	63.64
No TM & No DS	Yes	Yes	99.20	**5.55**	60.89	55.21
TM & No DS	Yes	No	99.33	1.39	62.87	54.53
TM & DS	No	N/A	99.04	1.39	43.07	47.83
TM & DS	Yes	Yes	**99.37**	3.78	37.62	46.92
TM & DS	Yes	No	99.37	3.58	35.15	46.03

Computation Times

This study explored the use of image processing to reduce the volume and variety of pixels classified by a supervised random forest classifier. To evaluate the speed-up enabled by these image processing methods, the central processing unit (CPU) time to perform each step in the classifier development was recorded. The time required to perform colour thresholding was negligible; since all methods explored in this study use colour thresholding, the time required to perform this step was constant for all methods, and so it is not included in the data presented here. All computations were completed on an Intel® Core™ i3-6300 CPU @3.70GHz dual-core processor with 4.00 gigabytes (GB) of random-access memory (RAM).

Table 2.5 contains the runtimes required to develop classifiers for each of the image processing methods. The method that did not use template matching nor de-speckling took the longest at almost 77 hours. The method using both template matching and de-speckling was the fastest at approximately 58 hours. In each of the methods that did not use template matching, generating features for the 50 images used to train and test the classifier took the longest. For the methods that used template matching, optimizing the template matching threshold took the longest to perform.

Table 2.5: Time required to develop hybrid classifiers for the four permutations of the template matching (TM) and de-speckling (DS) image processing procedures. Processing steps are ordered as the times taken to (1) optimize the template matching threshold, (2) generate features for the original 50 images, (3) perform recursive feature elimination, (4)

train a classifier using 10 features, (5) train a classifier using all 68 features, (6) test the classifier using 10 features, and (7) test the classifier using all 68 features. HH represents the number of hours, MI represents the number of minutes, and SS.SS represents the number of seconds taken to perform each step.

	Runtimes (HH: MI: SS.SS)			
Step	No TM & No DS	No TM & DS	TM & No DS	TM & DS
1	N/A	N/A	52:00:00.00	52:00:00.00
2	76:30:40.68	75:42:09.28	18:10:45.19	5:55:26.07
3	0:06:45.80	0:06:47.45	0:00:22.35	0:00:21.92
4	0:01:16.39	0:01:12.18	0:00:03.69	0:00:03.01
5	0:01:17.77	0:01:15.54	0:00:04.59	0:00:04.99
6	0:00:06.93	0:00:06.88	0:00:00.40	0:00:00.37
7	0:00:07.18	0:00:07.03	0:00:00.39	0:00:00.36
Total	76:40:14.74	75:51:38.36	70:11:17.00	57:55:56.70

Template matching significantly reduces the number of pixels that will need to be classified by the random forest; however, the cost of this work reduction is the need to tune the similarity threshold value used by the template-matching method. Tuning this threshold for one image using the EER method described above took approximately 2 hours. In this study, the optimal value of this parameter was calculated by performing the EER method on the 50 images used for generating the training and testing sets. The distribution of the resulting 50 threshold values was approximately normal, with a mean of 0.25 and a standard deviation of 0.017. Using these values to estimate the required number of images to optimize the value of the similarity threshold within the 90%, 95%, and 99% confidence intervals resulted in estimates of 18, 26, and 45 images, respectively. Table 2.6 shows the approximate time required to estimate the similarity thresholds for these numbers of images. For the remainder of this discussion, it will be assumed that a 95% confidence interval around the true value of the similarity threshold is acceptable, and thus, the time required to estimate this parameter will be 52 hours—the time required to perform the EER method on 26 images.

Table 2.6: Estimated number of images required to achieve a given level of confidence in the estimated similarity threshold, and the associated computation time required to perform the EER-based optimization of the threshold.

Confidence Interval (%)	Number of Images	Approximate Runtime (Hours)

99	45	90
95	26	52
90	18	36

Table 2.7 shows the time required for each of the 8 hybrid classification methods to fully classify an unseen image. As can be seen in these data, the classification speed increases with increased image processing. The hybrid classification methods that combined template matching with de-speckling performed the fastest, running on average in under 1 second per image, where the methods not utilizing template matching required on average more than 15 seconds to complete.

Table 2.7: The average time required to classify an image for each of the 8 hybrid classification methods explored in this study. All methods include colour thresholding as a pre-processing step. HH represents the number of hours, MI represents the number of minutes, and SS.SS represents the number of seconds taken to perform each step.

Image Processing	Feature Selection	Runtimes (HH: MI: SS.SS)
Template Matching & De-Speckling	No	0:00:00.96
Template Matching & De-Speckling	Yes	0:00:00.97
Template Matching & No De-Speckling	No	0:00:05.00
Template Matching & No De-Speckling	Yes	0:00:05.01
No Template Matching & No De-Speckling	Yes	0:00:15.64
No Template Matching & De-Speckling	Yes	0:00:15.74
No Template Matching & No De-Speckling	No	0:00:16.17
No Template Matching & De-Speckling	No	0:00:16.24

DISCUSSION

The objective of this study was to evaluate image processing as an effective way to improve supervised classification of an invasive species within un-calibrated high-resolution aerial RGB imagery. Because of the large number of pixels that compose each image, and the relatively small amount of information available from the un-calibrated red, green, and blue values recorded for each pixel, it is expected that proper image processing will improve the overall classification accuracy as it will allow the classifier to focus on discriminating pixels with a smaller variety of characteristics. Furthermore, by reducing the total number of pixels

to be processed by supervised classification, we expect that judicious use of image processing will significantly improve the speed with which an image can be classified.

Due to the colour, shape, and size of YFI patches, it can be difficult to distinguish them from background vegetation based solely on the properties of foliage. In the application of distinguishing YFI from other vegetation based only on foliage, spectral features would likely be replaced by shape and textural features to improve classifier performance. In the studies performed by Dronova et al. (2012), Jones et al. (2011), and Mitchell et al. (2016), it was found that clustering was effective in isolating ground cover types, specific vegetation types, and vegetation species. However, these applications were conducted in areas where the objects of interest were primary features in the images being studied. In many of the images used in this study, YFI was present only in small proportions. Pérez-Ortiz (2016) found the method of clustering basic ground cover types to be effective in initially removing non-vegetative areas from an image, after which point, clustering could be performed on the newly masked image to further distinguish unique vegetative species within the image. The resulting multi-stage clustering method required human intervention at the completion of each stage to assign a classification to each cluster. Such a method will not scale up to large regions with highly variable land cover, and thus was not explored in this study. Instead, classification of YFI was based on identifying its characteristic yellow flower and not attempting to identify the whole plant.

Environmental factors such as lighting, viewing angle, differences in physical attributes and clustering of YFI, and vegetation maturity caused high variability in the characteristics of YFI blooms in the images sampled in this study. As the template matching similarity threshold was optimized to reduce both the number of false positives and false negatives, plants that scored below the similarity threshold value were excluded from further classification. When coupled with the small size of YFI flowers in relation to image resolution, detection of YFI flowers through image analysis methods alone were ineffective. Edge detection methods were evaluated for defining areas of interest along water banks where YFI is commonly located; however, due to the marshy nature of the water bodies present, edge detection struggled to locate water boundaries. Instead, colour thresholding, coupled with template matching and/or de-speckling, was investigated as a method to

improve the classification of the image. These image processing steps served to reduce the volume and variety of the pixels that were then classified by a supervised random forest classifier.

In the study performed by Hill et al. (2017), it was found that using a supervised random forest classifier to classify pixels representing YFI flowers based on the un-calibrated RGB intensity values of the pixel alone resulted in high false positive results. For this reason, derived features calculated from a 9×9-pixel neighbourhood centred on the pixel of interest were used to support the supervised classification step. Although 68 features were derived from the RGB intensities, it is expected that some of them may represent redundant or misleading information for the random forest, for this reason feature selection was performed using the recursive feature elimination method, resulting in an optimal feature subset containing 10 features.

Accuracy can be a measure that considers the impact of both false positive and false negative classifications. As illustrated in Table 2.4, the method that combines colour thresholding with template matching and random forest classification based on the optimal feature subset provided the best results, with a classification accuracy of 99.4%. This represents a nearly 1.34% increase in accuracy over applying colour thresholding alone.

The precision values are all low, as shown in Table 2.4, with a maximum value of 5.5%. This indicates that all the methods considered in this study have a high number of false positive classifications. It can also be seen from these data that, except in one case, all the methods that use the random forest classifier as the final step in the classification have higher precision than the methods that do not use supervised classification. This suggests that supervised classification has a significant benefit for improving the classification based on the image processing alone by significantly reducing the number of false positives.

The sensitivity data, shown in Table 2.4, reveals that application of the colour threshold alone incorrectly classifies approximately 5% of the YFI in the image; however, it reduces the number of pixels that must be analysed by approximately 99%. The data presented in this table also suggest two breaks in the sensitivity values, one at approximately 75% and one at approximately 50%. The methods with sensitivity higher than 75% do not

use template matching as part of the processing of the image, whereas all the methods with a sensitivity lower than 25% combine both template matching with de-speckling. Only two methods, those that combine colour thresholding, template matching, and random forest classification, sit in the range of 75%–25% sensitivity. Template matching serves to reduce the sensitivity of the classification method; thus, it is incorrectly identifying YFI flowers in the image. This could be due to the selection of a poor template pattern of the flower to the effect of distortion caused by the perspective projection of the image, or to lighting conditions. This reduction of sensitivity could possibly be mitigated by placing a higher importance on recognizing false negatives over false positives when tuning the threshold parameter in template matching. However, when it is considered that template matching improved the overall accuracy, a metric that combines the impact of false positive and false negative classifications, it seems that a reduction in sensitivity is necessary to reduce the false positive rate to be more equal to the false negative rate.

In our previous work (Hill et al., 2017), false positives constituted a majority of the positive classifications of YFI in an image classified by a random forest classifier alone. Furthermore, all the hybrid classification methods developed in this study had a relatively high number of false positives, as indicated by the precision measures for each method. Thus, to be useful, a classification method will have to reduce the false positive rate. Based on the results found here, the most effective way to reduce the false positive rate while maximizing sensitivity is to apply image processing in the form of colour thresholding and de-speckling prior to the use of a random forest classifier. While it was found that the methods that used template matching and a random forest classifier provided the highest accuracy, it functioned to significantly reduce sensitivity.

Due to the high computational requirements involved in generating the derived features used to describe each image pixel, image processing methods that reduced the number of pixels that were to be classified by the supervised random forest classifier significantly reduced the time required to develop a classifier from training data and to use this classifier to evaluate a single image. While colour thresholding reduced the number of pixels to be considered by the random forest classifier most significantly, template matching came in second, and reduced the number of pixels much more substantially than did de-

speckling. Thus, the methods that included template matching could classify new images more quickly than methods that did not include template matching, with the template matching and de-speckling method taking on average 1 second to fully classify the image, and the template matching and no de-speckling method taking on average 5 seconds per image. In contrast, the methods that did not include template matching required over 15 seconds each to classify an image. While template matching did require the time-consuming step of optimizing the similarity threshold, this was a one-time step that did not need to be repeated for successive images. Thus, template matching will scale well as an image-processing step for the large number of images that are generated by high-resolution aerial imaging surveys by RPASs, and may be a viable solution for near-real-time image classification needed for adaptive management.

CONCLUSION

This study assessed the benefits of combining image processing with supervised classification to improve the performance of classification of an invasive weed captured in high-resolution imagery acquired by an un-calibrated RPAS-borne digital camera. By comparing 8 hybrid classification methods composed of permutations of the image-processing steps of template matching, de-speckling, and the use (or not) of feature selection in training a random forest classifier, we investigated how image processing can be most effectively used to improve image classifications in terms of accuracy, precision, sensitivity, and speed. Our results suggest that image processing can be combined with supervised classification to significantly improve overall classification accuracy at the expense of decreased sensitivity. However, this decreased sensitivity is balanced by a significant reduction in false positive classifications. Our results also suggest that the type of image processing used must be carefully considered, because over-processing of the image serves to reduce the overall performance of image classification.

The best hybrid image-processing/random forest classification method identified in this work demonstrated an overall accuracy, precision, and sensitivity of 99%, 4.8%, and 93%, respectively, on a validation data set comprising 20 images not used in the method's creation. This hybrid method required approximately 16 seconds to classify a 4608-pixel by 3456-pixel image on an Intel® Core™ i3-6300 CPU @3.70GHz with 4.00 GB of RAM. This

classification performance represents a significant improvement over our previous results (Hill et al., 2017) and suggests that digital cameras carried aboard consumer-grade RPASs have immense potential to improve the accuracy of invasive species mapping. Inexpensive equipment such as the DJI Phantom 3 Pro used in this study is increasingly accessible to invasive species practitioners; however, the large number of high-resolution aerial images captured during an aerial survey of even a modestly sized region is overwhelming for manual image analysis. The hybrid classification method developed here presents a pathway for automated image classification that will help scale such analyses to larger spatial regions and potentially enable adaptive management based on RPAS-acquired imagery.

REFERENCES

Adam, E., Mutanga, O., & Rugege, D. (2010). Multispectral and hyperspectral remote sensing for identification and mapping of wetland vegetation: a review. *Wetlands Ecology and Management*, *18*(3), 281-296.

Creston Valley Wildlife Management Area. (n.d.). Retrieved September 14, 2017 from https://www.crestonwildlife.ca/habitat/description.

Dronova, I., Gong, P., Clinton, N. E., Wang, L., Fu, W., Qi, S., & Liu, Y. (2012). Landscape analysis of wetland plant functional types: The effects of image segmentation scale, vegetation classes and classification methods. *Remote Sensing of Environment*, *127*, 357-369.

Fawcett, T. (2006). An introduction to ROC analysis. *Pattern Recognition Letters*, *27*(8), 861-874.

Fernandes, M. R., Aguiar, F. C., Silva, J. M., Ferreira, M. T., & Pereira, J. M. (2014). Optimal attributes for the object based detection of giant reed in riparian habitats: A comparative study between Airborne High Spatial Resolution and WorldView-2 imagery. *International Journal of Applied Earth Observation and Geoinformation*, *32*, 79-91.

GNU Image Manipulation Program. (n.d.). Retrieved September 23, 2017 from https://www.gimp.org.

Havel, J. E., Kovalenko, K. E., Thomaz, S. M., Amalfitano, S., & Kats, L. B. (2015). Aquatic invasive species: challenges for the future. *Hydrobiologia*, *750*(1), 147-170.

Hawthorne, T. L., Elmore, V., Strong, A., Bennett-Martin, P., Finnie, J., Parkman, J., ... & Reed, J. (2015). Mapping non-native invasive species and accessibility in an urban forest: A case study of participatory mapping and citizen science in Atlanta, Georgia. *Applied Geography*, *56*, 187-198.

Hill, D. J., Tarasoff, C., Whitworth, G. E., Baron, J., Bradshaw, J. L., & Church, J. S. (2017). Utility of unmanned aerial vehicles for mapping invasive plant species: a case study on yellow flag iris (Iris pseudacorus L.). *International Journal of Remote Sensing*, *38*(8-10), 2083-2105.

Jones, D., Pike, S., Thomas, M., & Murphy, D. (2011). Object-based image analysis for detection of Japanese knotweed sl taxa (Polygonaceae) in Wales (UK). *Remote Sensing*, *3*(2), 319-342.

Kraaijenbrink, P. D. A., Shea, J. M., Pellicciotti, F., De Jong, S. M., & Immerzeel, W. W. (2016). Object-based analysis of unmanned aerial vehicle imagery to map and characterise surface features on a debris-covered glacier. *Remote Sensing of Environment*, *186*, 581-595.

Lawson, E., Smith, D., Sofge, D., Elmore, P., & Petry, F. (2017). Decision forests for machine learning classification of large, noisy seafloor feature sets. *Computers & Geosciences*, *99*, 116-124.

Ma, L., Cheng, L., Li, M., Liu, Y., & Ma, X. (2015). Training set size, scale, and features in Geographic Object-Based Image Analysis of very high resolution unmanned aerial vehicle imagery. *ISPRS Journal of Photogrammetry and Remote Sensing*, *102*, 14-27.

Malanson, G. P., & Walsh, S. J. (2013). A geographical approach to optimization of response to invasive species. In *Science and Conservation in the Galapagos Islands* (pp. 199-215). Springer, New York, NY.

Mathews, A. J. (2014). Object-based spatiotemporal analysis of vine canopy vigor using an inexpensive unmanned aerial vehicle remote sensing system. *Journal of Applied Remote Sensing*, *8*(1), 085199.

Michez, A., Piégay, H., Lisein, J., Claessens, H., & Lejeune, P. (2016). Classification of riparian forest species and health condition using multi-temporal and hyperspatial imagery from unmanned aerial system. *Environmental Monitoring and Assessment*, *188*(3), 146.

Mitchell, M., Wilson, R. R., Twedt, D. J., Mini, A. E., & James, J. D. (2016). Object-based forest classification to facilitate landscape-scale conservation in the Mississippi Alluvial Valley. *Remote Sensing Applications: Society and Environment*, *4*, 55-60.

Moranduzzo, T., Melgani, F., Mekhalfi, M. L., Bazi, Y., & Alajlan, N. (2015). Multiclass coarse analysis for UAV imagery. *IEEE Transactions on Geoscience and Remote Sensing*, *53*(12), 6394-6406.

Moranduzzo, T., & Melgani, F. (2014). Detecting cars in UAV images with a catalog-based approach. *IEEE Transactions on Geoscience and Remote Sensing*, *52*(10), 6356-6367.

Pérez-Ortiz, M., Peña, J. M., Gutiérrez, P. A., Torres-Sánchez, J., Hervás-Martínez, C., & López-Granados, F. (2016). Selecting patterns and features for between-and within-crop-row weed mapping using UAV-imagery. *Expert Systems with Applications*, *47*, 85-94.

Pyšek, P., & Richardson, D. M. (2010). Invasive species, environmental change and management, and health. *Annual Review of Environment and Resources*, *35*.

Qian, H., & Ricklefs, R. E. (2006). The role of exotic species in homogenizing the North American flora. *Ecology Letters*, *9*(12), 1293-1298.

Rodriguez-Galiano, V. F., Ghimire, B., Rogan, J., Chica-Olmo, M., & Rigol-Sanchez, J. P. (2012). An assessment of the effectiveness of a random forest classifier for land-cover classification. *ISPRS Journal of Photogrammetry and Remote Sensing*, *67*, 93-104.

Stone, K.R. (2009). *Iris pseudacorus*. Fires Effects Information System. U.S. Department of Agriculture, Forest Service, Rocky Mountain Research Station, Fire Sciences Laboratory. http://www.fs.fed.us/database/feis

Yu, N., Li, L., Schmitz, N., Tian, L. F., Greenberg, J. A., & Diers, B. W. (2016). Development of methods to improve soybean yield estimation and predict plant

maturity with an unmanned aerial vehicle based platform. *Remote Sensing of Environment*, *187*, 91-101.

Zhu, Z., Gallant, A. L., Woodcock, C. E., Pengra, B., Olofsson, P., Loveland, T. R., ... & Auch, R. F. (2016). Optimizing selection of training and auxiliary data for operational land cover classification for the LCMAP initiative. *ISPRS Journal of Photogrammetry and Remote Sensing*, *122*, 206-221.

Chapter 3: Monitoring Grassland Invasion by Spotted Knapweed (Centaurea maculosa) with RPAS-Acquired Imagery

INTRODUCTION

Invasive plants are exogenous species that have been introduced to new environments, rapidly altering the structure and function of host ecosystems, and homogenizing the existing biotic communities (Pyšek & Richardson, 2010; Qian & Ricklefs, 2006). These changes to ecosystems caused by plant invasions can result in significant negative environmental impacts (Powell, Chase, and Knight, 2011; Davis, 2003). Treatment of invaded sites is therefore critical in mitigating this outcome. Early detection and mapping of the extent of invasion has been found to be beneficial and cost-effective when treating invasions (Malanson & Walsh, 2013; Holden, Nyrop, and Ellner, 2016).

With the introduction of remotely piloted aircraft systems (RPASs) as a remote sensing platform, there has been increasing interest in using this technology for the detection of biological invasions (Baron, Hill, and Elmiligi, 2018; Hill et al., 2017; Sandino et al., 2018; Alvarez-Taboada, Paredes, and Julián-Pelaz, 2017). RPASs have shown promise for improving land-cover mapping (Kalantar et al., 2017), vegetation mapping for invasive species detection (Hill et al., 2017), agricultural monitoring of crop health (Candiago et al., 2015), and evaluations of crop yield and maturity (Yu et al., 2016). Central to the problem of mapping biological invasions using remote sensing is the ability to accurately distinguish invasive plants from backdrop vegetation. Previous work has explored the impacts of increased spatial resolution and timing of data collection to leverage unique physiological features that are associated with a plant's phenological stage (Huang & Asner, 2009; Müllerová, Pergl, and Pyšek, 2013), and increased spectral resolution to leverage differences in narrow band reflectance for discriminating between vegetation types (Lass et al., 2002). It has been shown that overall accuracy (OA, the percentage of correct classifications relative to the total number of classifications) of the classification is affected by the composition of invading plants. Monospecific patches with higher vegetation cover present a clear spectral signature that can be leveraged by the classifier to produce higher accuracies. On the other hand, the spectral reflectance of a mixed communities blends the spectral signatures of the

plants present within a specific area; obfuscating the signature of the target species and degrading the classifier performance (Michez et al., 2016). Furthermore, the availability of accurate training data is a limiting factor in classifier performance, as the amount of training data available has been shown to have a large impact on classification accuracy when selecting a classifier (Huang, Davis, and Townshend, 2002), and poor data quality can confound classifiers during training.

Spotted knapweed (*Centaurea maculosa*) is a perennial, tap-rooted plant native to central Europe and east-to-central Russia, where it grows in relatively low densities as part of grassland ecosystems (Sheley, Jacobs, and Carpinelli, 1998). It is highly invasive in North America, dominating both rangeland and grasslands, which has made it a target of study and control for over four decades (Carson, Bahlai, and Landis, 2014). In its native environment, spotted knapweed cultivates soil biota that inhibit its further growth, but in North American grasslands, the soil conditions produced by spotted knapweed promote its growth (Callaway et al., 2004). This positive feedback mechanism reduces overall biological diversity and influences the relative abundance of species within invaded grassland communities (Klironomos, 2002). This plant–soil interaction pattern, coupled with the long-term viability of dormant seeds (Davis et al., 1993), renders spotted knapweed a particularly virulent invasive species in North America that can require long-term management.

The overall objective of this study was to develop a multispectral image analysis method suitable for mapping an invasive herbaceous plant—spotted knapweed—within a semi-arid grassland ecosystem. This is challenging because both the native perennial grasses (e.g., bunchgrasses) in this ecosystem and the invasive spotted knapweed have small leaves, stems, and stalks. Additionally, the ecosystem is characterized by high plant species diversity.

Object-based image analysis (OBIA) permits the use of spatially derived texture features such as grey level co-occurrence matrix (GLCM) -based metrics (Haralick, Shanmugan, and Dinstein, 1973; Jensen, 2015), metrics used to evaluate the co-occurrence of pixel grey level values at given offsets, to enhance image classification. It has shown immense promise for species level-classification of forest canopies (Blaschke, 2010; Blashcke et al., 2014). Application of OBIA, however, generally requires that the pixel size be small, relative to the objects (e.g., plant structural features, such as leaves) within the

scene, a condition that is difficult to achieve given the small physical size of grassland plants. On the other hand, traditional pixel-based image analysis methods accommodate images in which the pixels are much larger than the objects within the scene; however, this type of image analysis more often utilizes texture features for generalized ground-cover mapping rather than object delineation. Additionally, due to the diversity of plants present and the similarity of the spectral signatures of healthy native grassland varieties, both to each other and to spotted knapweed in the visible and near infrared (NIR) bands, multispectral imagery contains insufficient information to distinguish invasive species from backgrounds of similar vegetation (Dewey, Price, and Ramsey, 1991; Woolley, 1971) using pixel-based methods. Much denser hyperspectral data has been shown to provide adequate information for detecting spotted knapweed in a grassland ecosystem (Lawrence, Wood, and Sheley, 2006); however, such data is costly to acquire.

This study develops a method that can leverage multispectral imagery to predict the relative abundance of spotted knapweed across the landscape by applying OBIA to contrived objects (which we call metapixels) representing quadrats, a unit area used by grassland ecologists to measure species composition. Specifically, this study aims to (1) develop the metapixel-based image analysis method for use in grassland environments where the spatial resolution is insufficient to segment the image into physical objects present in the scene, and (2) explore the utility of incorporating GLCM-based texture metrics as features in metapixel-based image analysis for predicting the relative abundance of spotted knapweed in an arid grassland ecosystem. The next section describes the metapixel-based method in detail and the field data collected to evaluate its performance. Next, results from feature selection, parameter tuning, and classifier performance are presented, followed by a discussion of these results. The paper concludes with a summary of key findings and implications for future work.

STUDY SITE

The area investigated in this study is the Laurie Guichon Memorial Grasslands Interpretive Site (LGMGIS), located south of Merritt, British Columbia (BC), Canada. The LGMGIS covers 100 hectares (ha) in the Western Cordillera physiographic region of Canada and is within the Interior Douglas Fir dry hot subzone of BC's biogeoclimatic ecosystem

classification system. Three field sites were selected within the LGMGIS, where the study was conducted. Each field site is approximately 1ha in size, with a gentle slope and southern aspect.

METHODS

All analyses were performed using Anaconda, a free and open-source distribution of the Python Programming Language, with the Scikit-Image 0.14.1 image processing libraries (Van der Walt et al., 2014), and the Scikit-Learn 0.20.1 machine learning libraries (Pedregosa et al., 2011). The R statistical computing environment (R Core Team 2018), utilizing the raster (Hijmans, 2019) and rgdal (Bivand, Keitt, and Rowlingson, 2019) packages, was used for data management and statistical analyses. ArcGIS software ArcMap 10.5.1 (ESRI, 2018) was used for map generation and visible inspection of image orthomosaics. Pix4D photogrammetry software version 4.1.25 (Pix4Dmapper, 2018) was used for image orthorectification, mosaicking, and georeferencing.

Image Acquisition and Data Preparation

Field data were collected at 93 $1m^2$ quadrats, 31 per site, on July 12, 2018. Plant species inventories were conducted within each of the quadrats by visual inspection, recording plant species present and the approximate percent canopy cover of each plant species within the quadrat boundaries. The locations of the quadrats were selected in March 2018, before emergence of vegetation, by walking within the site boundaries and tossing markers at random intervals and directions. The markers, consisting of 70cm segments of steel reinforcement bar (rebar) were then driven into the ground where they landed to a depth of 60cm. These markers were used to define the south-west corner of $1m^2$ quadrats that were aligned with the cardinal (North/South and East/West) directions. Six of the markers at each site functioned as ground control points (GCPs). These markers were fitted with a 12.7cm diameter, high-visibility safety-orange cap. Geographic coordinates of all marker locations were determined using an iSXBlue 2+ GPS receiver. The iSXBlue receiver uses a satellite-based augmentation system (SBAS) that combines a geographic positioning system (GPS) with GPS correction data received from the United States' wide area augmentation system (WAAS) to achieve horizontal accuracies below 60cm twice the distance root mean square

(2dRMS) at the 95% confidence level. Location of the quadrats within field site 1 and an image of a typical quadrat acquired on July 04, 2018 are illustrated in Figure 3.1.

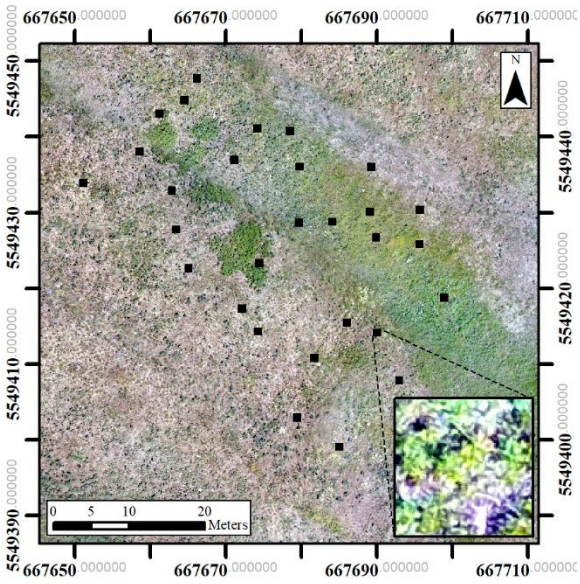

Figure 3.1: Locations of field quadrats at field site 1 shown in the WGS UTM Zone 10N coordinate system, and an overlaid close-up view of a typical quadrat captured by the 16-megapixel digital camera integrated in the Sequoia sensor.

RPAS imaging flights were conducted between the hours of 11:00a.m. and 1:00p.m. on July 04, July 12, and July 19, 2018. Images were acquired by a Parrot Sequoia sensor, equipped with a 16-megapixel digital camera, four 1.2-megapixel global shutter single-band imagers, an incident light sensor, and a global positioning system (GPS), carried aloft by a DJI Phantom 4 quadcopter. The sensitivity of the single-band imagers of the Sequoia sensor are provided in Table 3.1. A flight height of 30m above ground level at the take-off location was selected to maximize spatial resolution while maintaining a safe flight plan. Flights were conducted in compliance with Canadian Aviation Regulations, qualifying for exemptions from a Transport Canada issued Special Flight Operations Certification (SFOC), generally required when flying an RPAS for commercial or research purposes at the time of collection (Transport Canada, 2018). All flights were conducted with the characteristics listed in Table 3.2.

Table 3.1: Technical specifications for the Parrot Sequoia sensor, including band number, band name, centre wavelength, and full width, half maximum (FWHM).

Band Number	Nominal Reflectance	Centred Wavelength	FWHM (nm)
1	Green	550	40
2	Red	660	40
3	Red Edge	735	10
4	NIR	790	40

Table 3.2: Flight parameters when performing data acquisition.

Height Above Ground Level(m)	Forward Overlap (%)	Side Overlap (%)	Time of Day	Max Wind Speed (km/h)
30	80	80	11:00a.m.-1:00p.m.	40

Images acquired by each of the Sequoia's single-band imagers assign a digital number (DN) to each pixel within the scene. These digital numbers are related to the radiance ($Wm^{-2}sr^{-1}$) reflected by the land surface over the pixel footprint according to the following equation (Parrot, 2017):

$$\boldsymbol{L = f^2 \frac{(DN - B)}{(A\varepsilon\gamma + C)}} \quad (1)$$

where, $\boldsymbol{DN}$ is the digital number recorded for each pixel; $\boldsymbol{\varepsilon}$ is the exposure time of the image in seconds, $\boldsymbol{\gamma}$ is the ISO; $\boldsymbol{f}$=2.2 is the f-number of the imager, which represents the ratio of the focal length to the aperture diameter of the lens; and $\boldsymbol{A, B}$ and $\boldsymbol{C}$ are calibration coefficients. These values are recorded in the exchangeable image file (EXIF) metadata at the time of image acquisition.

Simultaneously with image acquisition by the single-band imagers, the incident light sensor of the Sequoia sensor measures a radiance level $\boldsymbol{\Psi}$, which is related to the irradiance $\boldsymbol{E}$ ($Wm^{-2}sr^{-1}$) received by the land surface over the pixel footprint according to the following equation (Tu et al., 2018):

$$\boldsymbol{E} = a\frac{\boldsymbol{\Psi}}{\boldsymbol{G\Gamma}} \quad (2)$$

where a is a constant, $\boldsymbol{\Psi}$ is the radiance level measured by the sensor, $\mathbf{G}$ is the sensor gain, and $\boldsymbol{\Gamma}$ is the measurement acquisition time. The values $\boldsymbol{\Psi}$, $\mathbf{G}$ and $\boldsymbol{\Gamma}$ are recorded in the EXIF metadata of the image at the time of image acquisition.

Surface reflectance ($\boldsymbol{\rho}$) is calculated during post processing of the images from the single band imagers using the following equation (Tu et al., 2018):

$$\boldsymbol{\rho} = \mathbf{K}\frac{\boldsymbol{L}}{\boldsymbol{E}} \quad (3)$$

where, $\boldsymbol{L}$ is calculated from the image pixel and EXIF metadata using equation 1, $\boldsymbol{E}$ is calculated using equation 2 and measurements from the incident light sensor stored in the image EXIF data, and **K** is a normalization constant that represents the ratio of the solid angles subtended from the incident light sensor to the solid angle subtended from each pixel within the imager and includes the constant a in equation 2. The normalization constant **K** is estimated during each flight using data from a ground-based, calibrated reflectance target. Following the manufacturer's recommended procedure, a calibration target specially designed for use with the Sequoia sensor was deployed adjacent to the location of take-off and landing and images containing the calibration target were captured prior to and immediately following the scheduled flight plan. During data processing, the calibration target is automatically detected in the Sequoia imagery by the Pix4D software. Because the calibration target's reflectance is known, equation 1, 2 and 3 can be used to estimate the value of the normalization constant (**K**) from the image pixels corresponding to the calibration target.

Metapixel-Based Image Analysis

Due to the small physical size of grassland vegetation, the wide variety of plants that live in grassland communities, and the potential for bare soil to be visible through the canopy, grassland composition is commonly expressed in terms of percent cover of dominant species types. Percent cover is a spatially averaged characteristic that is commonly measured

in the field, and, in this study, it was evaluated at the $1m^2$ scale using a quadrat-based approach. Taking inspiration from this approach for measuring grassland composition, we performed a chessboard segmentation to split each image orthomosaic into a set of non-overlapping squares, which we call metapixels and use as objects for OBIA. The size of the metapixels was selected to be consistent with the size of the quadrats used for the field data collection (i.e., $1m^2$) to avoid representativeness issues that would result from changing the spatial support of the relative abundance calculation between the field- and image-based methods. Features describing each metapixel can then be derived from the spectral reflectance values of each pixel falling within the bounds of the metapixel.

In this work 84 features were derived to describe each metapixel. The mean and standard deviation of pixel-level reflectance values for each spectral band constitute eight features. The mean and standard deviation of three multiband spectral indices calculated for each pixel falling within the bounds of the metapixel constitute another six features, and the remaining 70 features are composed of GLCM-based texture features calculated for each of the five spectral bands and three multiband indices.

Three multiband spectral indices, adaptations of the normalized difference vegetation index (NDVI), were calculated for each pixel within the metapixels. Each index was calculated by comparing NIR to each remaining spectral reflectance bands. Spectral indices calculated using the red and NIR band reflectance values are labelled NDVI. Indices comparing the green and NIR band reflectance values are labelled gNDVI. Indices comparing the red-edge and NIR band reflectance values are label reNDVI. Each index was calculated as:

$$\mathbf{NDVI} = \frac{\boldsymbol{\rho_{NIR}} - \boldsymbol{\rho_{R}}}{\boldsymbol{\rho_{\mathrm{NIR}}} + \boldsymbol{\rho_{R}}} \tag{4}$$

$$\mathbf{gNDVI} = \frac{\boldsymbol{\rho_{NIR}} - \boldsymbol{\rho_{G}}}{\boldsymbol{\rho_{NIR}} + \boldsymbol{\rho_{G}}} \tag{5}$$

$$\mathbf{reNDVI} = \frac{\boldsymbol{\rho_{NIR}} - \boldsymbol{\rho_{RE}}}{\boldsymbol{\rho_{NIR}} + \boldsymbol{\rho_{RE}}} \tag{6}$$

where $\boldsymbol{\rho_G}$, $\boldsymbol{\rho_R}$, $\boldsymbol{\rho_{RE}}$, and $\boldsymbol{\rho_{NIR}}$ stand for the values of the green, red, red-edge, and NIR spectral reflectance values.

For each metapixel, the following GLCM-based texture metrics were computed from the pixel-level values for each of the four spectral bands measured by the Sequoia imager and for each of the three multiband indices: angular second moment (ASM), correlation, entropy, sum entropy, and difference entropy. ASM is a measure of homogeneity of the image, correlation is a measure of grey-tone linear-dependencies in the image, entropy measures the disorder within an image (and is inversely proportional to the ASM), sum entropy measures the sum of the entropies across pixels, and the difference entropy measure the difference of entropies across pixels. These GLCM-based texture metrics were selected because they are invariant under grey-tone transformation (Haralick, Shanmugan, and Dinstein, 1973), and thus, are expected to be less sensitive to changes in irradiance during imaging (e.g. as caused by intermittent cloud cover) and sensor calibration errors. Texture features for each spectral band and multiband index within a metapixel were calculated from GLCMs representing the co-occurrence of pixel grey levels within a 1-pixel neighbourhood in the vertical (0°), horizontal (90°), diagonal-up (45°), and diagonal down (135°) directions. These directional relationships were defined as being reciprocal, so, for example, co-occurring grey-levels in both the up and down position constitute a vertical co-occurrence relationship. Thus, for each metapixel four directional variants of each GLCM are computed and each matrix is symmetric. ASM, correlation, sum entropy, entropy, and difference entropy were calculated using each directional GLCM; resulting in four directional texture values, which were generalized using their mean and range statistics. The mean and range statistics were selected because they are invariant under rotation of the metapixel (Haralick, Shanmugan, and Dinstein, 1973), and thus constitute omnidirectional versions of the GLCM-based spatial statistics. Rotation invariant GLCM-based spatial statistics were chosen to increase the generalizability of these features across a landscape where geographic features (e.g., aspect, breaklines, and ridges) are not expected to be co-aligned. This process generates 70 aggregate GLCM-based texture features for each metapixel, namely, the mean and range of the directional ASM, correlation, sum entropy, entropy, and difference entropy texture metrics for each of the four spectral bands and three multiband indexes.

Training data were created by defining each surveyed quadrat as a metapixel in the image, calculating the 84 spectral and textural features for this metapixel and labelling these features with the field measured species abundance of the quadrat. These data were used to train a random forest classifier to predict the percent cover of the target species based on the spectral and textural signature of each metapixel.

Image Processing

RPAS images were georeferenced and mosaicked with Pix4Dmapper photogrammetry and RPAS mapping software, an implementation of the structure-from-motion (SfM) algorithm (Turner, Lucieer, and Watson, 2012). Georeferencing of the orthomosaicked images created by Pix4D, based on coordinates acquired by the global navigation satellite system (GNSS) embedded in the imaging sensor and recorded in the EXIF data of the image, can be considered a 1^{st} order approximation due to error in the GNSS positioning system (on the order of 10m). To improve spatial registration across data acquisition dates, the GCPs (6 per site) were used for final georeferencing of the image orthomosaic. The digital camera data was not considered in this study and only the orthomosaics generated from data acquired by the four calibrated single-band sensors were selected for further analysis. The ground-resolved distance (GRD) of the single-band orthomosaics created by Pix4D is 2.9cm.

Field survey locations were used to mask the orthomosaics and extract georeferenced sub-images for each surveyed quadrat. This mask was created by first visually identifying the markers defining the south-west corner of each quadrat within the orthomosaic and then manually digitizing a square snapped to the location of the marker and extending 1 metre in the north and east directions. Because of the 60cm accuracy of the GPS used in this work, visual identification of the markers, rather than GPS-acquired location coordinates, was used to define the sub-image mask to ensure that the extracted sub-images corresponded as closely as possible to the physical quadrat analysed in the field. Each extracted sub-image corresponds to a $1m^2$ metapixel for which the species composition was measured by field survey and comprises 1156 pixels (34 rows by 34 columns). In total 868 sub-images were generated representing 93 metapixels across four spectral bands collected on July 04, 2018,

62 metapixels across 4 bands on July 12, 2018 due to sensor failure at field site 1, and 62 metapixels across 4 bands on July 19, 2018 due to sensor failure at field site 2.

Data Compilation

Due to the high variability of spotted knapweed density encountered in the field-surveyed quadrats relative to the number of quadrats surveyed, it was necessary to convert the percent cover measurements into qualitative classes representing increasing degrees of spotted knapweed cover. This was done to increase the number of examples representing each degree of spotted knapweed cover, a necessary consideration for training a classifier. The number of classes was selected based on two criteria: (1) there should be enough classes to show relative abundance and distribution over space, and (2) classes should be general enough to compensate for under-represented concentrations of spotted knapweed sampled during data collection. Based on these criteria, three non-overlapping classes of spotted knapweed relative abundance were created. Sixty-seven sites were identified where spotted knapweed was not present or only present in trace amounts, these were classified as “None”. Eighty-seven sites were identified where concentrations did not exceed 25% cover, these were classified as “Moderate”. Sixty-seven sites were found exceeding 25% cover and were classified as “High”.

The data was then split into training data and a validation set. The validation set was comprised of the data collected from site 3 on July 04, 2018, while the remaining data was used for training. Because balanced training sets have been shown to improve classifier performance (Zhu et al., 2016), these training data were sampled to create a balanced set of training examples. This was done using stratified random sampling, where the minority class is over-sampled while the remaining classes are down-sampled to match the sample size of the limiting class (Ma et al., 2015). Classifier performance was evaluated during training using 10-fold cross-validation, a training method that is suitable for quantifying training error in stochastic classifiers, such as random forests. During 10-fold cross validation, the data was randomly partitioned into 10 non-intersecting subsets of equal size folds by random sampling. The classifier was then trained 10 times, each time reserving one of the subsets as a validation set on which to evaluate the classifier error, while training the classifier using the remaining 9 subsets. The classifier with the lowest mean squared error among the 10 trained

classifiers is selected for the final model, and the accuracy of this model on the training set, referred to as the cross-validation score, is calculated as the average accuracy overall 10-folds of the training process.

Feature Selection

To evaluate the importance of the GLCM-based texture metrics for metapixel-based image analysis, we compared the performance of the method using the full set of 84 potential features, comprising the mean and standard deviation value of each of the four spectral bands and three multi-band indices and the mean and range values of the five texture features for each spectral band and index (hereafter referred to as the "GLCM-enhanced" version of the method) to a method restricted to the 14 potential features representing the mean and standard deviation value of each of the 4 spectral bands and 3 multi-band indices (hereafter referred to as the "no-GLCM" version of metapixel-based image analysis).

For both versions of metapixel-based image analysis performed in this study, recursive feature elimination was used to identify the optimal feature subset. Recursive feature elimination was performed by training random forest classifiers (Breiman, 2001) for both the no-GLCM and GLCM-enhanced versions of the method. Features were sorted based on feature importance, and the classifiers were retrained recursively removing the single least important feature from the sorted list. This process was repeated iteratively to find the best performing subset of features (Pedregosa et al., 2011) and the optimum feature subset for each classifier was recorded.

Classification

A random forest classifier was selected for this study based on its extensive use in remote sensing applications (Baron, Hill, and Elmiligi, 2018; Michez et al., 2016; Marceau et al., 1990; Breiman, 2001). This work employed a multi-class, single-output classifier to predict the percent cover of spotted knapweed, the target invasive species, at each image metapixel. Figure 3.2 illustrates the image classification workflow.

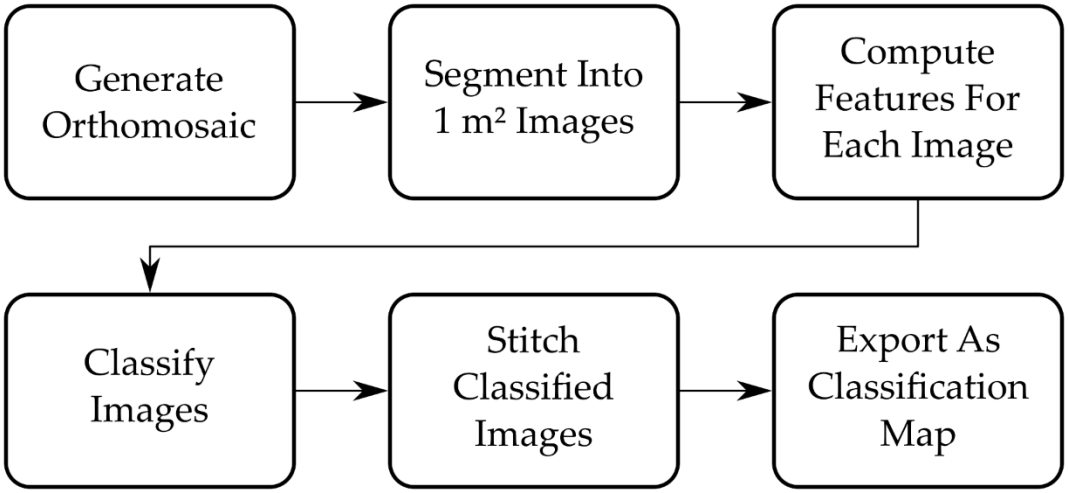

Figure 3.2: Image classification workflow used in this study.

The classifiers used in the no-GLCM and GLCM-enhanced versions of metapixel-based image analysis were trained using 10-fold cross-validation on training datasets with the optimal feature subsets identified for that classifier through recursive feature elimination. Hyperparameter tuning was then performed on the classifiers. Hyperparameter tuning began with a random search cross-validation method as a computationally efficient means of approximating hyperparameter values, followed by a grid search cross-validation method on a refined search area to identify the optimum hyperparameter values for the random forest classifier (Pedregosa et al., 2011). The optimized classifiers' performances were evaluated using the mean cross-validation accuracy scores, and the performance of the optimized classifiers were verified by testing the tuned classifiers on the validation data set. The parameters optimized for the random forest classifiers developed for both versions of metapixel-based image analysis explored in this study are summarized in Table 3.3.

Table 3.3: Definitions of the parameters used when optimizing the random forest classifier.

Parameter	Definition
n_estimators	Number of trees in the forest.
max_depth	Maximum depth of the tree.
min_samples_split	Minimum number of samples required to split an internal node.
min_samples_leaf	Minimum number of samples required to be at a leaf node.

max_features	Number of features to consider when looking for the best split.
bootstrap	Whether bootstrap samples are used when building trees.

RESULTS

Metapixel-Based Image Analysis without Texture Features

The classifier developed for the no-GLCM version of metapixel-based image analysis was trained using 14 features, namely the mean and standard deviation values of the pixel-level spectral reflectance and multiband indices contained within the $1m^2$ quadrats. The mean cross-validation score for a classifier trained using all 14 features was 62.7%. The optimum feature subset identified by recursive feature elimination contained 10 of the 14 possible features. The selected features were 1) mean green reflectance, 2) standard deviation green reflectance, 3) standard deviation red reflectance, 4) mean red-edge reflectance, 5) standard deviation red-edge reflectance, 6) mean NIR reflectance, 7) standard deviation NIR reflectance, 8) mean gNDVI reflectance, 9) standard deviation gNDVI reflectance, and 10) mean reNDVI reflectance. The mean cross-validation score improved slightly, when compared to the classifier trained using the full feature set, to 64.0%. Hyperparameter tuning of the random forest classifier using the optimized feature set resulted in another small gain in performance achieving a mean cross-validation score of 68.0%. Optimized hyperparameter values for the metapixel-based classifiers are presented in Table 3.4. When applied to the validation set, the classifier achieved an accuracy of 55.7%. Classification results for each stage of optimization are presented in Table 3.5.

Table 3.4: Parameters found through hyperparameter tuning of the classifiers developed for the no-GLCM and GLCM-enhanced versions of metapixel-based image analysis. A max features value of ‘sqrt’ indicates that the maximum number of features to use is the square root of the total number of features.

Version	n estimators	max depth	min samples split	min samples leaf	max features	Bootstrap
no-GLCM	196	90	7	1	‘sqrt’	FALSE

GLCM-enhanced	528	80	2	1	‘sqrt’	FALSE

Table 3.5: Performance of the classifiers developed for the no-GLCM and GLCM-enhanced versions of metapixel-based image analysis. Performance metrics include: mean 10-fold cross-validation accuracy scores for the initial un-optimized classifiers, the intermediary classifiers optimized through feature selection, the final classifiers optimized through feature selection and hyperparameter tuning, and the accuracy of the final classifiers when tested on the validation set.

Version	Un-optimized (%)	Feature Optimized (%)	Hyperparameter & Feature Optimized (%)	Validation Set Accuracy (%)
no-GLCM	62.7	64.0	68.0	55.7
GLCM-enhanced	58.0	68.7	71.3	66.0

Metapixel-Based Image Analysis with Texture Features

The classifier developed for the GLCM-enhanced version of metapixel-based image analysis was initially trained using the full set of 84 features. The mean cross-validation score of the classifier when using all 84 features was 58.0%. The optimum feature subset identified by recursive feature elimination contained 19 of the 84 possible features. The selected features were 1) mean green ASM, 2) mean green sum entropy, 3) mean green entropy, 4) mean green difference entropy, 5) range green ASM, 6) range green correlation, 7) range green sum entropy, 8) standard deviation red reflectance, 9) mean red difference entropy, 10) range red entropy, 11) mean red-edge reflectance, 12) mean red-edge entropy, 13) range NIR ASM, 14) range NIR sum entropy, 15) mean NDVI sum entropy, 16) range NDVI sum entropy, 17) standard deviation gNDVI reflectance, 18) range gNDVI sum entropy, and 19) mean reNDVI reflectance. The mean cross-validation score improved substantially (68.7%), when compared to the classifier trained using the full feature set. Hyperparameter tuning of the random forest classifier using the optimized feature set resulted in another gain in performance achieving a mean cross-validation score of 71.3%. Optimized hyperparameter values for this classifier are presented in Table 3.4. When applied to the validation set, this

classifier achieved an accuracy of 66.0%. Classification results for each stage of optimization are presented in Table 3.5. A classification map derived from applying this classifier to the orthomosaicked image from field site 3 on July 04, 2018, the image selected as the validation set, can be seen in Figure 3.3.

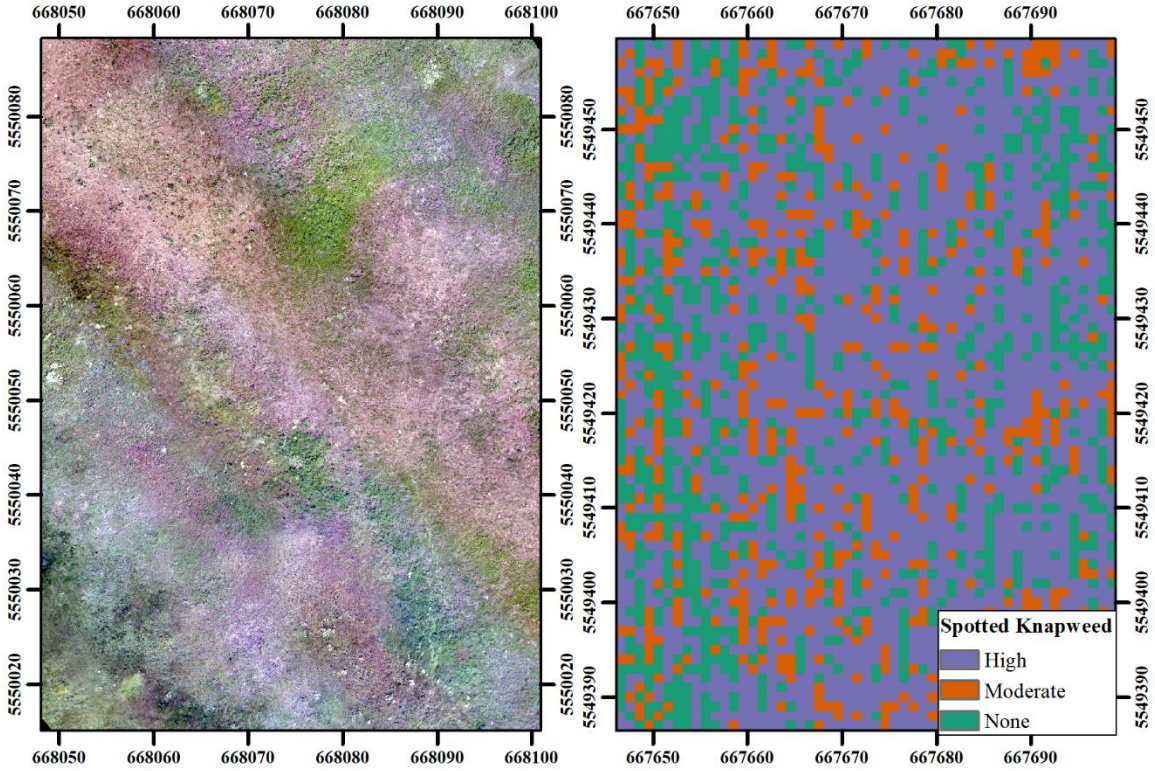

Figure 3.3: Orthomosaic generated from flight data collected at field site 3 on July 4, 2018 (left), and the classification map (right) generated using GLCM-enhanced metapixel-based image analysis using the optimized and tuned random forest classifier , which displays the relative concentrations of spotted knapweed. Images are projected in the WGS UTM Zone 10N coordinate system.

Model Generalizability

The performance of GLCM-enhanced metapixel-based image analysis was further explored to evaluate its ability to classify areas spatially distant from the area used for model development by developing three additional classifiers to evaluate model generalizability across sites. Using a leave-one-out approach, classifiers were trained on each combination of two sites following the workflow defined in Figure 3.2 and validated using the third unseen

site. For each combination of training sites, feature selection and hyperparameter tuning was performed to improve classification performance. The results of analysis are presented in Table 3.6.

Table 3.6: Performance of GLCM-enhanced metapixel-based image analysis developed using training data from each combination of two field sites and tested on the third, held-out site. The performance metrics of classifier performance and validation score correspond to the mean 10-fold cross-validation accuracy scores for classifiers optimized through feature selection and hyperparameter tuning, and the accuracy of the final classifiers when tested on the unseen validation site, respectively.

Training Sites	Test Site	Classifier Performance (%)	Validation Score (%)
1, 2	3	66.7	64.9
1, 3	2	69.2	56.0
2, 3	1	73.3	68.0

The performance of these classifiers, trained using a substantially smaller set of examples, show similar results to those obtained using a subset of data from all three sites for training. For each binary grouping of sites, the optimized classifiers performed well during cross-validation and when applied to data from the held-out site.

DISCUSSION

The objective of this study was to develop and evaluate a multispectral image analysis method suitable for identifying the extent of spotted knapweed invasion within a semi-arid grassland ecosystem. The metapixel-based image analysis method developed in this work took inspiration from grassland field surveys to quantify relative abundance of the target species, in terms of percent cover, within square reference units which we termed metapixels. Metapixel-based image analysis can be considered a type of OBIA, where the objects are not physical objects visible within the image scene, but rather contrived objects necessary to calculate spatially averaged measures of land cover, such as percent cover. It was necessary to develop the metapixel-based image analysis method because neither OBIA, based on a segmentation of the image into physical objects present in the scene (e.g. by edge-based segmentation), nor pixel-based methods could be readily applied to estimate the

relative abundance of spotted knapweed present within the image orthomosaics produced in this study. The 2.9cm spatial resolution of the Sequoia images was insufficient to resolve the physical characteristics of individual spotted knapweed plants and could not support edge or region-based methods to segment the image into constituent objects. The image resolution was also insufficient to provide examples of pixels representing pure spectral signatures of spotted knapweed, among other vegetation present within the scene, and thus pixel-based methods could not be applied without data from field-spectrometry or a spectral library to provide the spectral signatures of the vegetation present within the scene. Additionally, the metapixel-based approach enabled the calculation of GLCM-based texture metrics, which substantially increased the data density of the 4-band multispectral imagery used in this study.

To evaluate the performance of metapixel-based image analysis for identifying the relative abundance of spotted knapweed, we applied it to RPAS-acquired multispectral imagery and field data collected at three sites located in the semi-arid grasslands of BC, Canada. The multispectral imagery comprised 4-bands, green, red, red-edge, and NIR. These bands were considered both on their own, and as part of three multiband indices to calculate 84 spectral and textural features for each metapixel. To gauge the importance of the GLCM-based features (i.e., ASM, correlation, entropy, sum entropy, and difference entropy), we compared the performance of metapixel-based image analysis using GLCM-based texture features (GLCM-enhanced) to metapixel-based image analysis that did not use GLCM-derived features (no-GLCM).

The results show that a random forest using the entire set of 84 features generated by the GLCM-enhanced method performed marginally with a mean cross-validation score of 58.0%, while the no-GLCM analysis performed comparably, exhibiting a mean cross-validation score of 62.7%. Feature optimization and hyperparameter tuning of the random forest used in the no-GLCM method provided a moderate increase in the performance of this method, resulting in a mean cross-validation score of 68.0%. However, this gain is primarily the result of hyperparameter tuning, as feature optimization of the no-GLCM method provided only a small increase in classifier performance. This result suggests that the mean and standard deviation of the spectral reflectance and multiband indices contain insufficient information to produce a robust classifier capable of classifying the relative abundance of

spotted knapweed within each metapixel. Thus, if pure pixel data were available to create a pixel-based classifier, this classifier would also struggle to identify the relative abundance of spotted knapweed within the image. This outcome corroborates previous work that suggested that multispectral imagery alone contains insufficient information for detecting spotted knapweed from a background of similar vegetation using pixel-based methods (Dewey, Price, and Ramsey, 1991; Woolley, 1971), and that more descriptive data, such as hyperspectral imagery is required to accomplish this objective (Lawrence, Wood, and Sheley, 2006).

The use of GLCMs enables the computation of additional descriptive features for each metapixel. However, when using this expanded feature set to build a classifier, feature optimization was required to achieve a classifier that outperformed classifiers that did not use GLCM-based features (i.e., those developed for the no-GLCM version of metapixel-based image analysis). Performing feature optimization and hyperparameter tuning together improved the mean cross-validation score for the GLCM-enhanced method to 71.3%. These results suggest that, by incorporating texture features, GLCM-enhanced metapixel-based image analysis improves classification performance over metapixel-based image analysis that does not use texture features for detection of a target species from a background of similar vegetation using multispectral imagery. Thus, the outcome of this study is significant because it suggests that metapixel-based analysis using GLCM-based texture features could provide an avenue for weed mapping using more readily accessible RPAS-acquired multispectral imagery.

As evidenced by the performance of GLCM-enhanced metapixel-based image analysis (66% validation score) over the no-GLCM version (56% validation score), the inclusion of GLCM-based texture features provided the most substantial improvement in our ability to detect the relative abundance of spotted knapweed. Given the variable levels of infestation across the study area and the ability of the GLCM-enhanced method to produce reasonably accurate results with a limited number of training data, we suspect that the unique physical structure of spotted knapweed can be characterized by the GLCM metrics considered in this study, despite the plant not being plainly visible within the orthomosaicked images. We attribute this to the distinct physical characteristics of spotted knapweed (e.g. thin, radially extending stems, frequent branching, and ovate bracts). The mean values of

ASM green, sum entropy green and entropy green were three of the most important features identified by feature selection. Both ASM and entropy are measures of orderliness of the intensity of the green reflectance within the metapixel (though they are inversely correlated). We suspect that the way spotted knapweed overlays background vegetation and bare soil within the metapixel reduces the orderliness of the green band grey level, decreasing the ASM green metric and increasing the entropy green metric, and that this behaviour is sufficiently characteristic of the relative abundance of spotted knapweed within a metapixel to aid in the metapixel's classification.

The initial, un-optimized feature set selected for the metapixel-based classifier using GLCM-based metrics was designed to provide a suite of features intended to be robust to the high environmental variability expected when capturing a natural scene. From the list of texture features presented in Haralick, Shanmugan, and Dinstein (1973), only features that were invariant under rotation and grey-tone transformation were explored. Features that vary with respect to rotation were avoided in attempts to improve the overall generalizability of a resulting classifier when introduced to new scenes where changes in hillslope angle, direction, and plant orientation within the landscape varied from examples provided in training data. Additionally, features invariant under grey-tone transformation were selected to compensate for possible changes in solar irradiance due intermittent cloud cover during data collection, changes in distance between imager and vegetation canopy across the imaged area, and difference between the calibration height and the true height of the imager over the canopy during the aerial survey due to topography, canopy, and wind. We suspect that by selecting only features invariant under rotation and grey tone transform, we provided the classifier with texture features that generalized well throughout the imaged area.

GLCM-based texture metrics are second-order spatial statistics describing the spatial relationship between pixels within a spatial neighbourhood. Thus, there is an underlying assumption of spatial and temporal stationarity of these statistics. Clearly spatial stationarity is required if the statistics are to characterize specific patterns across space, while temporal stationarity is required if the statistics are used to derive classifiers that are trained on historical data and applied to data collected at some point in the future. We did not test for spatial stationarity within or between our field sites, and, while it might be reasonable to assume spatial stationarity within each 100 m x 100 m field site, it is probably unreasonable

to assume that this stationary regime encompasses all three field sites, which are separated by a minimum and maximum centroidal distance of 160 m and 750 m, respectively. None-the-less, our results show that when trained on data sampled across all three sites, GLCM-based metrics did not degrade classifier performance, but rather improved the ability of the classifier to predict the relative abundance of spotted knapweed within metapixels across multiple sites. This could be because the random forest classifier used in this study is sufficiently expressive to model inter-site differences in the metrics or because the use of rotation and grey-tone transform invariant metrics coupled with the similarity between the field sites rendered the statistics stationary when calculated in the imaged areas.

To further explore the impacts of spatial extrapolation of GLCM-enhanced metapixel-based image analysis, we explored classifiers trained exclusively on examples from two of the field sites and validated the performance of the derived classifier on the third, held-out field site. The performance of these classifiers (average training score 70%, average validation score 63%) was very similar to the performance of the classifier trained using examples from all three sites (training score 71%, validation score 66%). In fact, when trained using the two nearest field sites (2 and 3) and validated against data from the most distant field site (1), which is over 500 m away, the method achieved the highest accuracy of all the classifiers developed in this study (training score 73%, validation score 68%). These results suggest that sufficient information was available from two of the field sites to classify relative abundance of spotted knapweed at a distant third site. These results also suggest that the GLCM-enhanced metapixel-based method can extrapolate from a small plot-scale training site to a larger field-scale mapping project. This is important, as often it is impractical to collect field data at spatially random locations across large regions, because some locations may have restricted access due to legal boundaries or fragile ecosystems (Hill et al., 2017).

The ability of the classifiers to extrapolate to the held-out field site without loss of performance suggests that the GLCM-based features are (at least approximately) stationary across the field sites Despite the distances separating them, the field sites were selected to be similar in terms of slope, aspect, and setting at the outset of the project. These sites are also all located within the same protected grassland and as such are subject to the same land management treatments. Additionally, by using only rotation and grey-tone transform

invariant GLCM-based statistics in defining our feature set, we selected statistics that are more likely to remain stationary within an image.

The performance of classifiers when approximating the relative abundance of spotted knapweed, despite limitations in both spectral and spatial resolution, suggest that this method is capable of providing qualitative estimates of infestation when monitoring targeted plant invasions in grassland ecosystems. Though unable to quantify areal coverage of spotted knapweed, the method produced estimates of relative cover within $1m^2$ quadrats. Using RPAS platforms to collect data over wide areas, this method could be used to monitor changes in the relative abundance of an invading species using a grid-based approach over wide areas, and track changes to invasion boundaries. Though traditional field-based data collection will produce more accurate estimates within quadrats, it is too laborious to be used for comprehensive coverage over even moderate areas. Based on the results of this study, we believe that this method used in conjunction with traditional field-based data collection will aid management strategies and planning through improved mapping of the extent of invasions and changes over time.

Based on the results of this study, we believe that further research into GLCM-enhanced metapixel-based image analysis is warranted. Overall, despite being unable to identify individual plants of the target species, it was able to perform basic detection and provide relative abundance estimates of spotted knapweed within the scene. Due to the high degree of spotted knapweed infestation within the study area, the use of spatial random sampling biased the training data towards classification of this category of relative abundance. Within these data, there were many more quadrats/metapixels characterized by a moderate spatial abundance of spotted knapweed than there were with no or high abundances. This is a known limitation of spatial random sampling in situations where there is a large difference in proportion between the class categories. Spatial stratified sampling could be used to ensure that there are enough examples of each class. However, creating a stratified sampling plan is impractical for invasive species mapping since it requires a priori knowledge of where examples of each category can be encountered within the study area.

To overcome the bias in the training data caused by spatial random sampling, we used a balanced sample to train the classifiers. This is only a partial solution, however, because there is a greater number of training examples for moderate spatial abundance, and thus, the

classifier was likely exposed to a greater variability of patterns for this class than for other classes during training. For this reason, the resulting classifier is expected to be better at classifying the moderate spatial abundance class than it is at predicting the other classes. Increasing the number of training data through additional field sampling would likely improve classification accuracy of the relative abundance of spotted knapweed.

A second limitation caused by the low number of examples of quadrats with no and high spatial abundance is that we were unable to use more than three categories (High (>25% cover), Moderate (<=25% cover), and None (<1% cover)) for the spatial abundance. Had there been more data across the range of degrees of infestation, we could have defined a larger number of narrower qualitative classes defining the relative abundance of spotted knapweed. Finally, due to the highly variable composition and concentration of backdrop vegetative species present within the scene, spatially random sampling did not provide sufficient training examples to attempt to predict relative abundance of other species in addition to spotted knapweed. In future work, sampling design should be carefully considered to ensure that there is sufficient data to train the classifier.

CONCLUSION

The metapixel-based analysis method proposed in this work proved suitable for mapping the relative abundance of spotted knapweed (*Centaurea maculosa*) in a highly diverse grassland ecosystem using four-band multispectral data captured with a RPAS. The relative abundance of knapweed in each metapixel was categorized into three qualitative classes, “High”, “Moderate”, and “None”, to increase the number of examples available to train the classifier using a balanced training set. Using metapixels to calculate texture features substantially increased the data density available from the four-band multispectral measurements. An evaluation of the benefits of feature optimization and hyperparameter tuning revealed that feature optimization is more significant than hyperparameter tuning in terms of improving the performance of the metapixel-based image analysis. With feature optimization and hyperparameter tuning, we were able to achieve a mean cross-validation score of 71.3% for classifying the relative abundance of spotted knapweed within the $1m^2$ metapixels. The optimal feature set identified included texture features representing first and second moments of both spectral reflectance and multiband indices.

Additionally, this study shows the importance of including GLCM-based texture metrics in metapixel-based image analysis. Inclusion of these features significantly improved the performance of the method for classifying spatial abundance of spotted knapweed across the study area. Due to the potential non-stationarity of GLCM-based statistics across a field site, we recommend using only rotation and grey-tone transform invariant GLCM-based statistics to increase the chance that approximate stationarity exists within the study area. In our study site, GLCM-enhanced metapixel-based image analysis extrapolated well to distances greater than 100m.

Finally, while this study has only considered the target species of spotted knapweed, the results of this study suggest that metapixel-based image analysis may be successful in mapping other grassland invasive species that are characterized by small physical size and spectral signature similarity to native grasses, such as cheatgrass. It also may be successful for mapping target forest species at the global scale using moderate-resolution multispectral imaging, such as is acquired by the moderate resolution imaging spectroradiometer (MODIS).

REFERENCES

Alvarez-Taboada, F., Paredes, C., & Julián-Pelaz, J. (2017). Mapping of the invasive species Hakea sericea using unmanned aerial vehicle (UAV) and WorldView-2 imagery and an object-oriented approach. *Remote Sensing*, *9*(9), 913.

Baron, J., Hill, D. J., & Elmiligi, H. (2018). Combining image processing and machine learning to identify invasive plants in high-resolution images. *International Journal of Remote Sensing*, *39*(15-16), 5099-5118.

Bivand, R., Keitt, T., and Rowlingson, B. (2019). *rgdal: Bindings for the 'Geospatial' Data Abstraction Library*. R package version 1.4-8. Retrieved June 24, 2020 from https://CRAN.R-project.org/package=rgdal

Blaschke, T. (2010). Object based image analysis for remote sensing. *ISPRS Journal of Photogrammetry and Remote Sensing*, *65*(1), 2-16.

Blaschke, T., Hay, G. J., Kelly, M., Lang, S., Hofmann, P., Addink, E., ... & Tiede, D. (2014). Geographic object-based image analysis–towards a new paradigm. *ISPRS Journal of Photogrammetry and Remote Sensing*, *87*, 180-191.

Breiman, L. (2001). Random forests. *Machine Learning*, *45*(1), 5-32.

Callaway, R. M., Thelen, G. C., Rodriguez, A., & Holben, W. E. (2004). Soil biota and exotic plant invasion. *Nature*, *427*(6976), 731-733.

Candiago, S., Remondino, F., De Giglio, M., Dubbini, M., & Gattelli, M. (2015). Evaluating multispectral images and vegetation indices for precision farming applications from UAV images. *Remote Sensing*, *7*(4), 4026-4047.

Carson, B. D., Bahlai, C. A., & Landis, D. A. (2014). Establishment, impacts, and current range of spotted knapweed (Centaurea stoebe ssp. micranthos) biological control insects in Michigan. *The Great Lakes Entomologist*, *47*(3 & 4), 3.

Davis, E. S., Fay, P. K., Chicoine, T. K., & Lacey, C. A. (1993). Persistence of spotted knapweed (Centaurea maculosa) seed in soil. *Weed Science*, 57-61.

Davis, M. A. (2003). Biotic globalization: does competition from introduced species threaten biodiversity? *Bioscience*, *53*(5), 481-489.

Dewey, S. A., Price, K. P., & Ramsey, D. (1991). Satellite remote sensing to predict potential distribution of dyers woad (Isatis tinctoria). *Weed Technology*, 479-484.

ESRI. (2018). *ArcGIS Desktop: Release 10*. Redlands, CA: Environmental Systems Research Institute.

Haralick, R. M., Shanmugam, K., & Dinstein, I. H. (1973). Textural features for image classification. *IEEE Transactions on Systems, Man, and Cybernetics*, (6), 610-621.

Hijmans, R.J. (2019). *raster: Geographic Data Analysis and Modeling*. R package version 3.0-7. Retrieved June 24, 2020 from https://CRAN.R-project.org/package=raster

Hill, D. J., Tarasoff, C., Whitworth, G. E., Baron, J., Bradshaw, J. L., & Church, J. S. (2017). Utility of unmanned aerial vehicles for mapping invasive plant species: a case study

on yellow flag iris (Iris pseudacorus L.). *International Journal of Remote Sensing*, *38*(8-10), 2083-2105.

Holden, M. H., Nyrop, J. P., & Ellner, S. P. (2016). The economic benefit of time-varying surveillance effort for invasive species management. *Journal of Applied Ecology*, *53*(3), 712-721.

Huang, C. Y., & Asner, G. P. (2009). Applications of remote sensing to alien invasive plant studies. *Sensors*, *9*(6), 4869-4889.

Huang, C., Davis, L. S., & Townshend, J. R. G. (2002). An assessment of support vector machines for land cover classification. *International Journal of Remote Sensing*, *23*(4), 725-749.

Jensen, J. R. (1996). *Introductory digital image processing: a remote sensing perspective* (No. Ed. 2). Prentice-Hall Inc.

Kalantar, B., Mansor, S. B., Sameen, M. I., Pradhan, B., & Shafri, H. Z. (2017). Drone-based land-cover mapping using a fuzzy unordered rule induction algorithm integrated into object-based image analysis. *International Journal of Remote Sensing*, *38*(8-10), 2535-2556.

Klironomos, J. N. (2002). Feedback with soil biota contributes to plant rarity and invasiveness in communities. *Nature*, *417*(6884), 67-70.

Lass, L. W., Thill, D. C., Shafii, B., & Prather, T. S. (2002). Detecting spotted knapweed (Centaurea maculosa) with hyperspectral remote sensing technology. *Weed Technology*, *16*(2), 426-432.

Lawrence, R. L., Wood, S. D., & Sheley, R. L. (2006). Mapping invasive plants using hyperspectral imagery and Breiman Cutler classifications (RandomForest). *Remote Sensing of Environment*, *100*(3), 356-362.

Ma, L., Cheng, L., Li, M., Liu, Y., & Ma, X. (2015). Training set size, scale, and features in Geographic Object-Based Image Analysis of very high resolution unmanned aerial vehicle imagery. *ISPRS Journal of Photogrammetry and Remote Sensing*, *102*, 14-27.

Malanson, G. P., & Walsh, S. J. (2013). A geographical approach to optimization of response to invasive species. In *Science and Conservation in the Galapagos Islands* (pp. 199-215). Springer, New York, NY.

Marceau, D. J., Howarth, P. J., Dubois, J. M. M., & Gratton, D. J. (1990). Evaluation of the grey-level co-occurrence matrix method for land-cover classification using SPOT imagery. *IEEE Transactions on Geoscience and Remote Sensing*, *28*(4), 513-519.

Michez, A., Piégay, H., Jonathan, L., Claessens, H., & Lejeune, P. (2016). Mapping of riparian invasive species with supervised classification of Unmanned Aerial System (UAS) imagery. *International Journal of Applied Earth Observation and Geoinformation*, *44*, 88-94.

Müllerová, J., Pergl, J., & Pyšek, P. (2013). Remote sensing as a tool for monitoring plant invasions: Testing the effects of data resolution and image classification approach on the detection of a model plant species Heracleum mantegazzianum (giant hogweed). *International Journal of Applied Earth Observation and Geoinformation*, *25*, 55-65.

Parrot. (2017). *Application note: Pixel value to irradiance using the sensor calibration model (SEQ-AN-01)*. Retrieved January 10, 2019 from https://forum.developer.parrot.com/uploads/default/original/2X/3/383261d35e33f1f375ee49e9c7a9b10071d2bf9d.pdf

Pedregosa, F., Varoquaux, G., Gramfort, A., Michel, V., Thirion, B., Grisel, O., ... & Vanderplas, J. (2011). Scikit-learn: Machine learning in Python. *the Journal of Machine Learning Research*, *12*, 2825-2830.

Pix4Dmapper. (2018). *Pix4D SA*. Retrieved July 07, 2018 from www.pix4d.com

Powell, K. I., Chase, J. M., & Knight, T. M. (2011). A synthesis of plant invasion effects on biodiversity across spatial scales. *American Journal of Botany*, *98*(3), 539-548.

Pyšek, P., & Richardson, D. M. (2010). Invasive species, environmental change and management, and health. *Annual Review of Environment and Resources*, *35*.

Qian, H., & Ricklefs, R. E. (2006). The role of exotic species in homogenizing the North American flora. *Ecology Letters*, *9*(12), 1293-1298.

R Core Team. (2018). *R: A Language and Environment for Statistical Computing*. Vienna: R Foundation for Statistical Computing. Retrieved July 07, 2018 from https://www.R-project.org/

Sandino, J., Gonzalez, F., Mengersen, K., & Gaston, K. J. (2018). UAVs and machine learning revolutionising invasive grass and vegetation surveys in remote arid lands. *Sensors*, *18*(2), 605.

Sheley, R. L., Jacobs, J. S., & Carpinelli, M. F. (1998). Distribution, biology, and management of diffuse knapweed (Centaurea diffusa) and spotted knapweed (Centaurea maculosa). *Weed Technology*, 353-362.

Transport Canada. (2018). *Qualifying for an exemption to fly a drone (current rules)*. Retrieved July 18, 2018 from http://www.tc.gc.ca/en/services/aviation/drone-safety/getting-permission-fly-drone-current-rules/qualifying-exemption-fly-drone-current-rules.html

Tu, Y. H., Phinn, S., Johansen, K., & Robson, A. (2018). Assessing radiometric correction approaches for multi-spectral UAS imagery for horticultural applications. *Remote Sensing*, *10*(11), 1684.

Turner, D., Lucieer, A., & Watson, C. (2012). An automated technique for generating georectified mosaics from ultra-high resolution unmanned aerial vehicle (UAV) imagery, based on structure from motion (SfM) point clouds. *Remote Sensing*, *4*(5), 1392-1410.

Van der Walt, S., Schönberger, J. L., Nunez-Iglesias, J., Boulogne, F., Warner, J. D., Yager, N., ... & Yu, T. (2014). scikit-image: image processing in Python. *PeerJ*, *2*, e453.

Woolley, J. T. (1971). Reflectance and transmittance of light by leaves. *Plant Physiology*, *47*(5), 656-662.

Yu, N., Li, L., Schmitz, N., Tian, L. F., Greenberg, J. A., & Diers, B. W. (2016). Development of methods to improve soybean yield estimation and predict plant maturity with an unmanned aerial vehicle based platform. *Remote Sensing of Environment*, *187*, 91-101.

Zhu, Z., Gallant, A. L., Woodcock, C. E., Pengra, B., Olofsson, P., Loveland, T. R., ... & Auch, R. F. (2016). Optimizing selection of training and auxiliary data for operational land cover classification for the LCMAP initiative. *ISPRS Journal of Photogrammetry and Remote Sensing*, *122*, 206-221.

Chapter 4: Summary and Conclusions

The use of RPASs and machine learning in remote sensing applications of invasive species mapping were shown to provide otherwise unobtainable information useful for planning and decision-making in land management. This study found that when used in conjunction with traditional field-based collection, these methods provided a more comprehensive visual representation of the target areas being studied than traditional point-based field data alone. There were distinct limitations across each method evaluated, however, these limitations can be addressed as the technologies available continue to develop and improve. By continuing to study ecosystems with this emerging technology, the extent of their capabilities can be better understood, methods for more efficient and effective land monitoring and management can evolve, and understanding of design limitations can hopefully affect the direction of further technological development to improve and meet the requirements of end-users.

In the study conducted for Chapter 2, pixel-based classification of raw, uncalibrated imagery provided an effective means for automatically detecting an invasive plant species that expressed a distinct spectral signature within the ecosystem. This can provide a means for quickly evaluating large areas captured by RPASs to evaluate the extent of invasion, distinct areas being invaded, and a means for easily identifying key areas of high concentration of the invading species. However, there were limitations to this work that could be immediately addressed and improved. First, data collection was conducted with an uncalibrated RGB camera. By utilizing a calibrated imager, the spectral signature of the target species would be more accurately recorded, reducing the number of conflicting data points that confound the classifier during training and testing. Second, raw imagery was used as orthomosaicks generated using the structure-from-motion algorithm did not retain sufficient detail to distinguish individual, unmixed examples of the target of interest. Unfortunately, this meant that outputs could not be easily adapted to a map for use in planning. This could be remedied by higher quality sensing equipment, such as a narrow swath imager that captures geo-rectified raw imagery that circumvents the need for the structure-from-motion algorithm, or by modifying the structure-from-motion algorithm to

handle orthorectification of additional non-spectral fields generated after image capture. Finally, increased spectral resolution (as provided by multispectral or hyperspectral imagers) could help better define the target of interest. Overall, the limitations found in this study may naturally be addressed as the technologies and their availability continue to improve.

In the study conducted for Chapter 3, predictions of the relative abundance of spotted knapweed provided a means for estimating total cover over large areas. This was performed in imagery where the target species was not clearly identifiable in orthomosaicks generated from multispectral imagery using the structure from motion algorithm. This analysis method could be best applied to tracking the boundaries of invasion, as well as the density of invasion within target areas. Major limitations to the effectiveness of this method are threefold. Classifiers developed to work with multispectral imagery alone struggled to distinguish the spectral signature of the target species in the diverse, grassland ecosystem, spatial resolution after generating orthomosaicks was too coarse to distinguish the structure of spotted knapweed, and considerable field-work was necessary to construct a training data set. Again, the biggest improvement to the overall effectiveness of this work would be to remove the need to rely on the structure-from-motion algorithm to generate an orthorectified image.

Remote sensing of invasive herbaceous plant species is difficult, as the size of the target species is often small relative to the spatial resolution of collected imagery. The end-goal of this study was to develop and evaluate methods for automating the detection of invasive plant species for mapping and land management purposes. Though the methods were unable to provide results reliable enough to entirely replace traditional field-based data collection, they do offer additional information useful for planning. As the technologies continue to develop and become more accessible, these methods and their reliability should continue to improve.